Article:

Marchev, P, Raicheva, R, Georgiev, S et al. (2 more authors) (2022) Formation of ultrapotassic magma via crustal contamination and hybridization of mafic magma: an example from the Stomanovo monzonite, Central Rhodope Massif, Bulgaria. Geological Magazine, 159 (1). pp. 81-96. ISSN 0016-7568

https://doi.org/10.1017/S0016756821000868

Formation of ultrapotassic magma via crustal contamination and hybridization of mafic magma: an example from the Stomanovo monzonite, Bulgaria

Journal:	*Geological Magazine*
Manuscript ID	GEO-21-2714.R1
Manuscript Type:	Original Article
Date Submitted by the Author:	n/a

Complete List of Authors:	Marchev, Peter; Geological Institute Strashimir Dimitrov Bulgarian Academy of Sciences Raicheva, Raya; Geological Institute Strashimir Dimitrov Bulgarian Academy of Sciences Georgiev, Stoyan; Geological Institute Strashimir Dimitrov Bulgarian Academy of Sciences Savov, Ivan; University of Leeds, School of Earth and Envinronment Jelev, Danko; Eastern Resources

Keywords:	ultrapotassic monzonite, green-core clinopyroxene, crystal-melt mixing, crustal contamination, Rhodope Massif

Abstract:	Generally all orogenic ultra-potassic (U-K) rocks are formed after melting of metasomatised sub-continental lithospheric mantle via crustal mica-bearing lithologies. Here we present another possible model, based on the study of the small Stomanovo U-K subvolcanic intrusion in the Central Rhodope Massif, Bulgaria. The Stomanovo monzonite porphyry straddles an age of a 30.50 ± 0.48 Ma and is intruded into the voluminous Oligocene (31.63 ± 0.40 Ma) Bratsigovo-Dospat felsic ignimbrite. The monzonite hosts both normally- and reversely-zoned clinopyroxene (CPX) phenocrysts. The normally-zoned CPX is characterized by gradually diminishing core-to-rim Mg# (89-74), whereas reversely-zoned CPX has green Fe-rich cores (Mg# 78-55) mantled by normally-zoned CPX (Mg #87-74). Neither the core of the normally-zoned CPXs, nor the Fe-rich green cores are in equilibrium with the host monzonite. This U-K monzonite shows more radiogenic Sr isotopes [(87Sr/86Sr)i =0.71066] and εNd(t) = (-7.8 to -8.0) that are distinct from ignimbrites with (87Sr/86Sr)i = (0.70917-0.70927) and εNd(t)= (-4.6 — -6.5). Isotopic data and the presence of copious zircon xenocrysts from the underlying metamorphic basement suggest extensive crustal assimilation. Our observations indicate that the Stomanovo U-K monzonite formed after extensive lower or middle crustal fractional crystallization from an evolved magma producing cumulates and their subsequent hybridization with primitive mantle-derived magma during continuous crustal contamination. We suggest that instead of inheriting their high K2O and LILE enrichments from slab-derived/metasomatic fluids, the Stomanovo U-K monzonite may owe at least some of its unusually high alkalinity to the assimilation of biotite-muscovite-K-feldspar from the metamorphic basement of the Rhodope Massif.

Formation of ultrapotassic magma via crustal contamination and hybridization of mafic magma: an example from the Stomanovo monzonite, Bulgaria

Peter Marchev[1], Raya Raicheva[1], Stoyan Georgiev[1], Ivan P. Savov[2], Danko Jelev[3]

[1] Geological Institute of Bulgarian Academy of Sciences, St. Acad. G. Bonchev bl. 24, 1113 Sofia, Bulgaria

[2] School of Earth and Environment, Institute of Geophysics and Tectonics, University of Leeds, Leeds LS2 9JT, United Kingdom

[3] Eastern Resources Ltd., Sofia, Bulgaria, 1000 Sofia, Bulgaria

Abstract

Generally all orogenic ultra-potassic (U-K) rocks are formed after melting of metasomatised sub-continental lithospheric mantle via crustal mica-bearing lithologies. Here we present another possible model, based on the study of the small Stomanovo U-K subvolcanic intrusion in the Central Rhodope Massif, Bulgaria. The Stomanovo monzonite porphyry straddles an age of a 30.50 ± 0.48 Ma and is intruded into the voluminous Oligocene (31.63 ± 0.40 Ma) Bratsigovo-Dospat felsic ignimbrite. The monzonite hosts both normally- and reversely-zoned clinopyroxene (CPX) phenocrysts. The normally-zoned CPX is characterized by gradually diminishing core-to-rim Mg# (89-74), whereas reversely-zoned CPX has green Fe-rich cores (Mg# 78-55) mantled by normally-zoned CPX (Mg #87-74). Neither the core of the normally-zoned CPXs, nor the Fe-rich green cores are in equilibrium with the host monzonite. This U-K monzonite shows more radiogenic Sr isotopes [$(^{87}Sr/^{86}Sr)_i$ =0.71066] and εNd(t) = (-7.8 to -8.0) that are distinct from ignimbrites with $(^{87}Sr/^{86}Sr)_i$ = (0.70917-

0.70927) and εNd(t)= (-4.6 — -6.5). Isotopic data and the presence of copious zircon xenocrysts from the underlying metamorphic basement suggest extensive crustal assimilation. Our observations indicate that the Stomanovo U-K monzonite formed after extensive lower or middle crustal fractional crystallization from an evolved magma producing cumulates and their subsequent hybridization with primitive mantle-derived magma during continuous crustal contamination. We suggest that instead of inheriting their high K_2O and LILE enrichments from slab-derived/metasomatic fluids, the Stomanovo U-K monzonite may owe at least some of its unusually high alkalinity to the assimilation of biotite-muscovite-K-feldspar from the metamorphic basement of the Rhodope Massif.

Keywords: ultrapotassic monzonite, green-core clinopyroxene, crystal-melt mixing, crustal contamination, Rhodope Massif

1. Introduction

Ultrapotassic (U-K) magmas (K_2O >3wt %; K_2O/Na_2O >2; Foley et al., 1987) are widely distributed among the collisional and post-collisional orogenic belts of the Mediterranean region (Boari & Conticelli, 2007; Prelević et al. 2008, 2012, 2015; Conticelli et al. 2009; Gülmez et al. 2016). They are predominantly lamproites, which are associated with leucite-bearing ultramafic rocks and more evolved trachytes, shoshonites and high-K calc-alkaline rocks (group III of Foley et al. 1987). As a rule, the mafic U-K magmas are characterized by more radiogenic isotope signatures with $^{87}Sr/^{86}Sr > 0.710$, which can be explained by melting of metasomatised sub-continental lithospheric mantle caused by interaction with sediment or continental crust- derived melts percolating through the upper mantle (e.g. Conticelli, 1998; Conticelli et al. 2009; Foley et al. 1987; Peccerillo & Martinotti, 2006; Prelević & Foley, 2007; Zhang et al. 2017; Förster et al. 2019). Such melts re-fertilize the otherwise refractory lithospheric mantle and help to establish new mineralogy and complex metasomatised vein networks (Foley, 1992; Müntener et al. 2001; Tomanikova et al. 2019).

Compared to other Mediterranean regions, the Paleogene U-K rocks in the Rhodope Massif are rare. Until recently, such rocks have only been recognized in the eastern Rhodopes, in particular from basaltic and trachyte lava flows from the periphery of the Oligocene Borovitsa caldera (Marchev et al. 1998, 2004; Yanev, 2003; Yanev & Ivanova, 2009). The petrogenesis of these rocks and their relationship with the wide spread shoshonites ($K_2O/Na_2O > 1$) remains as subject of controversy. Some authors have suggested the Eastern Rhodope U-K rocks were derived from a partially molten, phlogopite-bearing, metasomatized mantle source (Yanev & Ivanova, 2009), possibly re-fertilized by a subduction component (Kirchenbaur et al. 2012*a*), while the role of crustal contamination was considered minimal. Conversely, other authors, based on the variations of the isotopic data with crustal thickness in the Rhodopes, have argued that magma crustal contamination was indeed an important factor (Marchev et al. 1998, 2004).

Until recently, U-K rocks from the western Rhodope Massif have not been reported. A 2007 gold exploration project produced 15 drill holes within the hydrothermally altered Stomanovo prospect, located in the SE part of the Bratsigovo-Dospat volcanic district (Fig. 1). One of them (SV010; coordinates: 41°47'54.88" N; 24°22'55.75" E) intersected a monzonite porphyry interpreted as a shallow intrusion stock which was proposed to be the cause for the hydrothermal alteration observed at the surface (Harkovska & Velinov, 2002). Preliminary petrological studies of the monzonite porphyry (Marchev & Jelev, 2011), designated as monzonite from here onward, revealed that the rock contains high-Mg clinopyroxene (CPX) with inclusions of high-Fe green CPX, suggesting a rather complex magmatic evolution. Here we present new data, which include age determinations, whole rock and mineral major and trace element abundances, and Sr and Nd isotope ratios for these rare

U-K Stomanovo monzonites. We use these data to offer an alternative view on the K_2O and LILE enrichments characteristic for the U-K post-collisional magmatism globally.

2. Geological setting

The Rhodope Massif represents a major tectonic zone in the Alpine- Himalayan mountain belt of the Eastern Mediterranean region (Fig. 1 inset) occupying a large part of southern Bulgaria and northern Greece. It was actively involved in the Alpine orogeny, with nappe stacking and crustal thickening events, which may have started by the Late Jurassic (Papanikolaou, 2009; Krenn et al. 2010; Turpaud & Reischmann, 2010; Burg, 2012; Froitzheim et al. 2014) and lasted until the Late Cretaceous to Early Tertiary (Burg et al. 1990, 1996; Collings et al. 2016). The nappes were successively exhumed in the Middle Tertiary, followed by Late Eocene to Early Oligocene syn- and post-orogenic extension (Burg et al. 1990, 1996; Koukouvelas & Doutsos, 1990; Kilias et al. 1999; Bonev & Beccaletto, 2007). We use Janak et al. (2011) model, who separate 4 nappes: the Lower, Middle, Upper and Uppermost Allochthon.

The Lower Allochthon includes 3 orthogneiss dominated metamorphic domes- the Arda, Kesebir and Biala Reka, and the marble dominated Pangeon-Pirin dome. The protolith ages of the orthogneiss domes are Variscan and range between 328 and 300 Ma (Peytcheva & von Quadt, 1995; Ovtcharova et al. 2002; Peytcheva et al. 2004). The age of gneisses of the Pangeon-Pirin dome appear to be younger and fall between 291 and 270 Ma (P. Turpaud, unpub. Ph.D. thesis, Johannes-Gutemberg- Universität, Mainz, 2006). The rocks of the Middle Allochthon are heterogeneous, represented by amphibolitized ophiolites that are closely associated with marbles, ortho- and para-gneisses and eclogites. Their protolith ages vary from Neoproterozoic to Late Cretaceous (Turpaud & Reischmann, 2010; Liati et al. 2011; Collings et al. 2016; Miladinova et al. 2018). Relevant to our study are the biotite orthogneisses of Assenitsa and Startsevo units of the Middle Allochthon, which are Jurassic (163-134 Ma; Von Quadt et al. 2008; Turpaud & Reischmann, 2010). The Upper Allochthon crops out in the Serbo-Macedonian Massif (Vertiskos-Ograzhden unt), the Pirin mountains and in the eastern Rhodopes (incl. Kimi Complex; Mposkos & Krohe, 2006). The Vertiskos-Ograzhden unit is composed of orthogneisses with protolith ages of 460-426 Ma (Macheva et al. 2006; Himmerkus et al. 2009; Peytcheva et al. 2009); The Kimi unit consists of HP and UHP gneisses, marbles, eclogites, amphibolites and metaperidotites with Lower Cretaceous age (Krohe & Mposkos, 2002; Kirchenbaur et al. 2012*b*). The Uppermost Allochthon includes Jurassic (177-164 Ma) greenschist facies sedimentary and volcano-sedimentary rocks of the Circum Rhodope Belt (Koglin et al. 2007; Bonev et al. 2015).

From the Late Cretaceous to the Middle Eocene the Rhodope Massif was affected by widespread subduction-related and post- collisional magmatic activity represented by numerous felsic to mafic intrusions (Peytcheva et al. 1998; Kamenov et al. 1999; Marchev et al. 2006, 2013; Soldatos et al. 2008; Marchev & Filipov, 2012). This magmatism was followed by slab break-off and asthenospheric uplift in the Rhodopes, which caused heating, fast exhumation of the massif and core complex formation during 42-35 Ma. Following the core complex exhumation, steep faulting and wide-spread extension in the Late Eocene-Oligocene resulted in emplacement of large volumes of volcanic and plutonic rocks (34-30 Ma), covering almost the entire Rhodope Massif (Del Moro et al. 1988; Harkovska et al. 1989, 1998; Jones et al. 1992; Yanev, 2003; Marchev et al. 2005, 2013). Generally, this magmatism is divided into 3 zones: the eastern Rhodope Magmatic Zone, the Central Rhodope Magmatic Zone and the Struma Magmatic Zone (Harkovska et al. 1998; Marchev et al. 1998). Most of the subvolcanic bodies in the eastern Rhodope Zone are intruded into the volcanic cover forming volcano-plutonic associations (e.g., Madjarovo, Zvezdel, Borovitsa; Mavrudchiev et al. 1993) closely associated with Pb–Zn–Cu and Ag–Au deposits (Marchev et al. 2005). Much deeper and larger plutons, coeval with the volcanic eruptions, are known in the Struma Magmatic Zone in the western Rhodopes (e.g., Teshovo and Central Pirin plutons; Kolokotroni & Dixon, 1991; Soldatos et al. 1998; Filipov et al. 2017; Zagorchev et al. 2017).

3. Bratsigovo-Dospat volcanic area

The Bratsigovo-Dospat volcanic area occupies the westernmost part of the Central Rhodope Magmatic Zone and comprises the largest felsic ignimbrite complex in the Rhodopes, covering ~700 km^2 with ~200 km^3 of erupted material (Fig.1). The geology of the area was studied by Katskov (1980) and Kackov (1987), who reported two altered andesite dykes, intruded into the Bratsigovo-Dospat ignimbrites. These ignimbrites are underlain by a sedimentary succession of Late Eocene (Priabonian- Early Oligocene) breccia-conglomerates, sandstones, siltstones and lenses of limestones. All of the volcano-sedimentary associations are underlain by the Rhodopean metamorphic basement, represented by the amphibolites, marbles and gneisses of the Middle Allochthon and migmatised biotite and amphibole-biotite orthogneisses and eclogites of the Lower Allochthon (Arda dome; Fig.1a). The entire volcano-sedimentary succession can be examined north of the town of Devin, ~2 km south of the studied Stomanovo U-K monzonite intrusion. The age of the Bratsigovo-Dospat ignimbrite is determined by K/Ar dating of biotite as 32-30 Ma (Harkovska et al. 1998). In the southern part of the Bratsigovo-Dospat volcanic area, the ignimbrites directly overlay the Paleocene Elatia- Barutin- Buynovo granodiorite (55.93 ± 0.28 Ma; U/Pb zircon; Soldatos et al. 2008).

The Stomanovo monzonite is intruded into the Bratsigovo-Dospat ignimbrites and forms an alteration halo (Fig. 1c). Alteration products are described in detail by Harkovska and Velinov (2002) and Velinov et al. (2007), who report quartz-sericite-alunite and quartz-diaspore zones without mineralization. The alteration zone has an East-West elongated shape

(2.5×1 km) and, most probably, formed as the result of hydrothermal activity linked to the intrusion of the Stomanovo monzonite.

4. Sampling and analytical method

The Stomanovo monzonite is covered by only 10-12 m of altered ignimbrite. Three unaltered sections were selected from the SV010 drill core at depths of 62 m (SV010-62), 83 m (SV010-83) and 129 m (SV010-129).

The abundances of the major and selected low abundance trace elements (Sc, V, Cr, Co, Ni, Zn, Cu, Pb, Ga, Zr, Hf, Nb, U, Y, Th, Rb, Sr, Ba, La, Ce, Nd) were determined on fused and pressed pellets, respectively, using a Philips PW2400 spectrometer at the University of Lausanne. Freshly broken cross-sections of the fused pellets from the XRF analyses of samples (SV10-83 and SV010-129) were analyzed for trace and rare earth elements (Zr, Hf, Nb, Ta, U, Y, Th, Rb, Cs, Sr, Ba and REE), using a New Wave Research (NWR) Excimer 193 nm laser-ablation system UP-193FX attached to a Perkin-Elmer ELAN DRC-e inductively coupled plasma mass spectrometer (LA-ICP-MS) at the Geological Institute of Bulgarian Academy of Sciences (GI BAS) in Sofia. We used 100 μm laser beam diameter and 5 to 10 Hz repetition rate. The NIST 610 glass material was used for external calibration standard, and the XRF values for SiO_2 were used as internal standard and cross-checking.

Major elements in minerals were determined using a JEOL 870 SUPERPROBE at the University of Florence. A 15 keV accelerating potential, 10 nA beam current and 1 μm beam diameter were used. In situ concentrations of trace-element abundances in CPX, plagioclase, biotite and sanidine crystals were determined on polished thin sections using the LA-ICP-MS at the GI BAS, Sofia. The laser-spot diameter was 50 to 35 μm and the energy of laser ablation was 5-10 Hz and 8 – 10 J/cm^2. The NIST 610 glass standard was used for external calibration with SiO_2 and CaO from the microprobe measurements as internal standards for cross-checking.

Zircon crystals for age determination were extracted from sample SV10-129, hand-picked and fixed in epoxy resin before polishing. Cathodoluminescence (CL) images and back-scatter electron images (BSE) were taken at the University of Belgrade, and used to check the internal structure of individual zircon grains. U-Pb ages of zircons were subsequently measured at the LA-ICP-MS laboratory of the GI- BAS. The laser crater was set at 35 μm and GEMOC-GJ1 zircon was used as an external standard. Fractionation correction and results were estimated using GLITTER 4.0 software (Macquarie University).

Thermal Ionization Mass Spectrometry (TIMS) was used for the analysis of $^{87}Sr/^{86}Sr$ and $^{143}Nd/^{144}Nd$ isotope ratios. Strontium (Sr) and Neodymium (Nd) were extracted from unspiked rock powders that were dissolved first in ultrapure HNO_3: HF acid mixture (1:3), dried and re-dissolved in optima grade ultrapure HNO_3 acid producing clear final solutions. The rock digestions were followed by conventional ion-exchange chromatographic techniques (Sr Spec and LN Spec resins) in a clean lab at the University of Leeds, UK. Sr and Nd isotope ratios were measured on a Triton series (Thermo Scientific) multi-collector mass spectrometer running in static mode. The normalization ratio used for Sr fractionation correction was $^{86}Sr/^{88}Sr = 0.1194$ and for Nd it was $^{146}Nd/^{144}Nd = 0.7219$. Instrument errors for determinations of $^{87}Sr/^{86}Sr$ and $^{143}Nd/^{144}Nd$ are reported as 2σ. External precision (2σ) for Sr and Nd isotopic ratios from successive replicate measurements of standards were < 20 ppm for the NIST SRM-987 standard, and < 20 ppm for the La Jolla Nd standard.

5. U-Pb zircon ages

Recently Filipov et al. (2017) used LA-ICP-MS U-Pb zircon dating to show that the age of the host ignimbrites is between 30.93 ± 0.28 Ma and 30.55 ± 0.25 Ma. Here we report new results from the host ignimbrites and the Stomanovo monzonite using U-Pb in zircon dating (Supplementary Table S1). The CL images of the zircon grains selected for our study show either prismatic or rounded to ovoid shapes. They have typical oscillatory magmatic zonation (Fig. 2a, b) with some xenocrysts or cores, mantled by 30-80 µm overgrowths with planar zonation (e.g. Fig. 2c, e). Many crystals show irregular surface or small embayments, indicative of resorption (Fig. 2d). Our newly determined age for the host ignimbrite of 31.63 ± 0.40 Ma (Fig. 3a) is based on determinations of twelve zircon grains. The age we report here is nearly identical to the ages reported by Filipov et al. (2017). Nine zircon analyses from the monzonite yield a concordant $^{206}Pb/^{238}U$ age of 30.50 ± 0.46 Ma, interpreted as the time of crystallization of the intrusion (Fig. 3). These ages, along with the field relationships, indicate that the intrusion occurred shortly after the ignimbrite eruption.

6. Petrography and mineral chemistry

The Stomanovo U-K monzonite intrusion consists of visually undeformed rocks with porphyritic textures consisting of zoned plagioclase, K-feldspar, orthopyroxene, CPX and biotite, with accessory apatite, opaque minerals and zircons within a holocrystalline groundmass of plagioclase, sanidine and quartz.

6.a. Major element chemistry

Orthopyroxene is completely replaced by Fe-Mg hydrosilicates of the iddingsite-bowlingite group and was not analyzed as a result.

Clinopyroxene **(CPX)** is the most common mafic mineral and shows normally and reversely zoned major element compositions (Table 1). In the pyroxene quadrilateral they plot in the fields of diopside and augite (Fig. 4). Normally zoned CPX phenocrysts have a gradual core to rim decrease in Mg# (89-74) and Cr (3850-17 ppm; Fig. 5a). They also have low TiO_2 (0.35-0.17 wt %), Al_2O_3 (2.52-1.08 wt %) and Na_2O (0.32 -0.12 wt %) and also similar Ti/Al ratios (0.06-0.16). Reversely zoned CPX (Fig. 5b) have green Fe-rich cores with widely varying Mg# (78-55) and low Cr (118-24 ppm) and higher TiO_2 (0.81-0.72 wt. %), Al_2O_3 (3.29-3.02 wt%) and Na_2O (0.55-0.46 wt%) abundances. They are wrapped by normally zoned CPX mantle (Mg# 87-74), compositionally similar to the normally zoned CPX.

Plagioclase occurs as 2 populations (Supplementary Table S2): either as clear and normally zoned grains with An_{53-45} (Fig. 5c), or showing larger compositional variation (An_{67-25}) and sieved textured outer rims with abundant small glass inclusions (Fig. 5d).

Sanidine has a relatively homogeneous composition (Supplementary Table S2) $Or_{75.5-69.1}Ab_{26.2-21.0}$ $An_{1.1-2.1}$ $Cn_{2.8-1.2}$).

Mica (Supplementary Table S3) forms either phenocrysts or occurs as inclusions in the sanidine. It has Mg# (74.0-71.4), showing slight decreases from cores to rims and Mg# similar to outer rims of the normally-zoned CPXs. On the classification diagrams (not shown) it falls in the field of the phlogopite, close to the boundary with high-Mg biotite. The analyzed phlogopite is characterized by high TiO_2 (6.37-5.64 wt%), Al_2O_3 (14.2-13.3 wt%) and K_2O (10.04-9.18 wt%). The F content reaches up to 3.3 wt%.

Ilmenite which is enriched in Mn (6.0-6.4 wt%; Supplementary Table S3) forms small crystals, and also contains a small amount of MgO (0.2-0.5 wt%).

6.b. Trace element chemistry

Clinopyroxene. Normally zoned CPXs and the mantles of the green cores have similar trace element concentrations (Table 2), characterized by high Cr and Sc and low Ti. The green pyroxene cores have higher Ti, V, Rb, Zr, Nb, U, Th and distinctively higher REE abundances. The CI-normalized REE patterns of the normally zoned CPXs and the mantles of the green core CPXs (Fig. 6a) display parallel and generally convex-upward REE patterns peaking at Nd and Sm and decreasing from Pr to La and Gd to Lu. The most Mg rich cores have a small Eu* anomaly (0.91), increasing in the outer low Mg zones to 0.56. All green CPXs have more elevated REE abundances and a pronounced Eu* anomaly in the range 0.63-0.51, with one of them showing slightly enriched flat profile from La to Sm (Table 2; Fig. 6a). The PM-normalized trace element patterns of these two groups (Fig. 6b) are rather similar, with troughs in Ba, Nb, Ta, Sr, Zr, Ti and peaks at Cs, Th, U, Pb, Nd, Sm, but these features are more pronounced in the green cores.

Plagioclase and sanidine. The CI-normalised diagram (Fig. 6c) shows a decreasing trend from La to Sm and positive Eu anomaly. With few exceptions, the MREE and HREE are below detection limit. The PM-normalized trace element patterns (Fig. 6d) are characterized by enrichments in Sr and Pb and Ba (Supplementary Table S4).

MIca has high Rb, Ba, Sr, Pb and Nb contents (Supplementary Table S4). These values are similar or slightly higher than those in the compositionally similar trachytes from Campi Flegrei, Italy (Fedele et al., 2015).

7. Whole rock major and trace element composition

The whole rock compositions of the Stomanovo monzonite are presented in Table 3. The samples span a narrow compositional range for SiO_2 (56 to 59 wt. %), as well as for the other major elements. The monzonite has very high K_2O (5.7-6.2 wt. %) and relatively low Na (~2.2 wt.%) contents and K_2O/Na_2O ratios ranging from 2.6 to 2.9, thus showing ultrapotassic affinity (Foley et al., 1987). Considering the presence of phlogopite, the loss on ignition (LOI) is low (0.8 to 2.3 %) suggesting only weak alteration. On the SiO_2 vs. K_2O diagram (Fig. 7a) the samples plot in the field of high-K (shoshonitic) series. On the total alkali-silica (TAS) diagram (Fig. 7b), the samples classify as monzonites, falling close to the quartz-monzonite field. Using the classification scheme of Foley et al. (1987), the Stomanovo monzonites fall in the Group III orogenic ultrapotassic series (see Fig. 7c).

The Stomanovo monzonite has high Rb (~450 ppm) and Ba (2000-2600 ppm) contents, as well as low Nb (15.6-17 ppm). Their CI-normalized REE patterns (Fig. 8a) exhibit clear LREE enrichment (La_N/Yb_N=14.3-15.55), flat heavy REE (HREE) patterns (Tb_N/Yb_N= 1.7-2.1) and moderate negative Eu anomalies (Eu/Eu*=0.72-0.84) (Fig. 5a). In the PM-normalized multi-element diagram (Fig. 8b), the Stomanovo monzonite samples exhibit enrichments of large-ion lithophile elements (LILE: Cs, Rb, Ba, Th, U) and Pb, and negative high field strength element (HFSE; Nb-Ta and Ti) anomalies considered typical for orogenic ultra-K magmas (Foley et al. 1987).

8. Sr and Nd isotopes

Sr and Nd isotopic compositions of representative unaltered Stomanovo monzonite sample are given in Table 4 and shown in Fig. 9. The monzonite has relatively radiogenic $^{87}Sr/^{86}Sr$ (0.71062) and unradiogenic $^{143}Nd/^{144}Nd$ (0.51220-0.51219) ratios, corresponding to εNd_i of -7.8 to -8.0). In contrast, the host ignimbrite displays less radiogenic $^{87}Sr/^{86}Sr$ (0.70917-0.70927) and more radiogenic $^{143}Nd/^{144}Nd$ (0.51228-0.51238), εNd_i (-4.6 to -6.5) (Filipov et al. 2017).

9. Discussion.

9.a. Sources for the Stomanovo U-K monzonite

The most notable feature of the Stomanovo monzonite is the large diversity of mineral compositions that is impossible to achieve via simple fractional crystallization and thus suggests mixing of two components: (i) mafic magma, containing high Mg CPXs (Mg# 89-86) and (ii) green high-Fe- and high-Na CPXs, crystallizing before the high-Mg CPXs. In addition, we observe large quantity of zircon xenocrysts, demonstrating possible involvement of large volumes of crustal material from the underlying older basement.

CPX-melt Fe-Mg exchange equilibrium ($Kd_{Fe–Mg}$ ~ 0.27 ± 0.03; Putirka, 2008) was used to calculate the composition of the magma from which both types of CPX crystallized. Our results show that the high Mg # 89-86 cores and rims of the normally and the reversely-zoned CPX crystallized from mafic magmas with Mg # = 69-63. These Mg# are much higher when compared with the Mg# (55.9-53.3) of the whole rocks, signaling lack of equilibrium with the host magmas. CPX in equilibrium with such primitive mantle-derived melt, indicate significant mantle contribution to the source of Stomanovo monzonite. Such relationships have also been observed in the alkaline syenites from Armenia (Sokol et al. 2018). The rims of the phenocrysts with Mg # 74 have crystallized from differentiated magmas with lower Mg#s (~44), which is probably the composition of the magma at the place of solidification.

Green CPXs with Mg# 71-55, corresponds to highly fractionated magmas with Mg# 40-25. Such high-Fe green cores of reversely-zoned CPXs with enriched LREE are more typical for OIB alkaline basalts (e.g. Brooks & Prinzlau, 1978; Wass, 1979; Duda & Schmincke, 1985; Dobosi, 1989; Neumann et al. 1999; Shaw & Eyzaguirre, 2000; Marchev et al. 2006). CPX with such compositions are not common in convergent margins but have been found in shoshonitic and ultrapotassic rocks in Italy (e.g., Varekamp & Kalamarides, 1989; Di Battistini et al. 1999); Leucite Hill, Wyoming (Barton & van Bergen, 1981); North Kazakhstan (Zhu & Ogasawara, 2004) and Yangtze craton (Xu et al. 2003; Huang et al. 2010). Rare green CPX grains have been observed also in the high-K rocks from the eastern Rhodopes of Bulgaria (R. Raicheva, unpub, Ph.D. thesis, Geol. Inst. BAS, Sofia, 2013). The origin of the green high-Fe CPX has been interpreted as either: (1) cognate phases of high-pressure origin that crystallized from evolved magmas (Barton et al. 1982; Duda & Schmincke, 1985; Dobosi, 1989; Xu et al. 2003; Marchev et al. 2006); 2) locally metasomatized upper mantle or lower crustal wall rock (e.g., Brooks & Printzlau 1978; Wass, 1979; Barton & Bergen, 1981; Dobosi & Fodor, 1992; Huang et al. 2010; Jankovics et al. 2013;) or 3) xenocrysts from subducted continental materials (Zhu & Ogasawara, 2004).

The major compositional difference between the green CPX in most alkaline rocks and the Stomanovo green CPX is the lower Al_2O_3 in the latter. Compared to the high-Mg CPXs mantles, they have slightly higher Al_2O_3 (<3.3 wt.%) and overall higher trace element abundances, but Sr. Nevertheless, the green CPX and high-Mg CPX show similar PM-normalized and CI-normalized multi-element patterns (Fig. 6 a, b) suggesting crystallization from common parental magma. We suggest that differentiated orogenic magmas can crystallize as gabbroic (CPX-plagioclase) to clinopyroxenite cumulates in the lower crust. Such xenoliths, composed of compositionally similar green clinopyroxenes, have been described in the Oligocene alkaline basalts from eastern Rhodopes (Marchev et al. 2006; 2008). Intrusion of a later batch of mafic mantle-derived magmas into such cumulate rocks can trigger reaction and mixing between the melt and disrupted green Cpx.

9.b. Conditions of magma crystallization

The documented crystal-melt mixing events precludes the calculation of meaningful crystallization temperatures and pressures of the monzonite based on mineral-melt or mineral-whole rock equilibrium. Further, the use of two-pyroxene geothermometer is hindered by the complete alteration of the orthopyroxenes. However, we are able to estimate P-T conditions using compositionally similar CPX, coexisting with fresh orthopyroxene and high-Al amphibole, found in the coeval neighboring Mesta trachydacites (Marchev et al., *in prep.*). Two-pyroxene thermobarometer of Putirka (2008) for these rocks gave P ~ 3.8-4.5 kb (12-15 km) and T of ~ 1030 ºC. Similar pressure (P~4.6 kb, ~15 km) and slightly lower temperature (T ~938 ºC) was obtained, when we used clinopyroxene Mg core (Mg# 80) – whole rock pair from Stomanovo, applying Putirka (2008) equation 31 and 33, respectively. However, comparison of the CPX core composition with other similarly high Cr content (up to 3850 ppm) and very low Al_2O_3 (< 2.5 wt%) CPX, reported for websterites crystallized from primitive mantle melts at the base of volcanic arc crustal section in Alaska and the Jijal complex, Kohistan (Jan & Howie, 1981; De Bari & Coleman, 1989) suggest that the crystallization of the CPX might have happened at much higher pressure. Such CPX has also been obtained from the experiments of high-Mg andesites at pressure of 12 kb (Müntener et al. 2001). Therefore, the core of the Stomanovo high-Mg CPX may have crystallized in a much deeper magma chamber within the lower crust. Overgrowth relationship between green CPX and their high-Mg rims indicate that green CPX must have formed at pressures similar to or higher than those of the high-Mg CPX grains.

For the temperature of crystallization in the late stage, we use plagioclase-K-feldspar thermometer of Putirka et al. (2008) yielding much lower temperature of (810-890ºC). We interpret this temperature as reflecting the post-mixing shallow crustal to sub-surface conditions.

9.c. The role of crustal contamination

There is a general consensus that in continental arcs crustal contamination is an inevitable process and that more evolved magmas are complex hybrids of mantle-derived basaltic melts and crustal (cumulate) rocks (e.g., Hildreth & Moorbath, 1988; DePaolo et al. 1992; Davidson et al. 2005; McLeod et al. 2012 , Crummy et al. 2014). A surprising result of our study is the more radiogenic composition of $^{87}Sr/^{86}Sr_i$ (0.71062) and εNdi (-7.8 to -8.0) of the monzonite compared to the host felsic ignimbrites ($^{87}Sr/^{86}Sr$ i =0.7092-0.7094; εNdi=-6.6 to -4.6; Fig. 6; Filipov et al. 2017). A possible explanation is the derivation of the monzonite by melting of a thoroughly metasomatized mantle source by previously subducted crustal sediments. However, this suggestion is at odds with the large amount of zircon xenocrysts in the monzonite, suggesting that a more reasonable explanation is extensive crustal contamination.

From the total number of 25 dated zircons 44 % were xenocrysts. It is worth nothing that zircon xenocrysts are more abundant than in the host ignimbrites. These zircons fall into 4 major populations: (1) 51-39 Ma; (2) 261 – 271 Ma; (3) 466 Ma and (4) 857-552 Ma. The ages of the zircon xenocrysts can be easily correlated with the ages of the rocks from the local outcrops of the metamorphic basement of the Upper Allochton (462-426 Ma) and Lower Allochtons (345-261) of the Rhodope Massif. They are broadly similar to the spectrum of ages determined for the metamorphic core complexes of the entire Rhodope Massif (see the summary in Burg, 2012; Bonev et al. 2013; Abbo et al. 2020) and xenozircon age spectrums in other Oligocene magmatic rocks (e.g. Bonev et al. 2013; P. Filipov, unpub. Ph.D. thesis, Geol. Inst. BAS, Sofia, 2014). The youngest zircon xenocryst population (51-39 Ma) is similar in the age to the nearby Barutin-Buynovo pluton (56-42 Ma; Soldatos et al. 2008).

In conclusion, it appears that the most possible places where the majority of the crustal contamination occurred are the middle crustal magma storage regions (12-15 km), as derives from the conditions of crystallization and, perhaps, lower crustal and even shallow subvolcanic magma chambers. On the other hand, the coincidence of the ages of the xenozircons with those from the basement lithologies clearly indicates that the entrainment of the zircons in the magma occurred during the entire route from the middle crust to the surface. Crustal contamination of the magma can be enhanced by its small volume and alkaline affinity, as well as the high temperature of the mafic magmas. The small volume magma can easily entrain foreign material during its travel to the surface, whereas its higher temperature and alkaline character can facilitate dissolution and contamination processes (see also next section) due to the low melt viscosities and thus increased mobility in the crust.

The crustal contamination is evident also by the similarity of the whole-rock Sr-Nd isotope compositions of the Stomanovo monzonite and the Rhodope metamorphic rocks (Fig. 9). Quantification of the process generally is made by AFC (assimilation-fractional-crystallization) or simple mixing models. However, the large variety of zircon xenocrysts in the Stomanovo monzonite reveals the complex composition of the underlying basement and potential participation of different contaminants, making the selection of end-member values difficult. Similarly, selection of the primitive magma composition is problematic, due to the scarcity of exposed mafic magmas, and the common fractionation and/or crustal contamination recorded in the crust of the Rhodopes (Marchev et al. 2004). Thus, the process of crustal contamination is difficult to reconcile quantitatively by any simple two-component crust-magma interaction (bulk mixing or AFC) models (McLeod et al., 2012). Nevertheless, just to demonstrate the potential role of crustal contamination, we constructed an AFC model using the equations of DePaolo (1981). A high radiogenic gneiss from the Lower Allochton (sample RH346; N. Cornelius, unpub. Ph.D. thesis, Johannes-Gutemberg- Universität, Mainz, 2008), recalculated for 30 Ma and the least radiogenic absarokite (sample Bg109b) from the eastern Rhodopes (Kirchenbaur et al. 2012*a*) have been selected as possible end members. Details of the end member selection and the calculation are given as an electronic appendix (Supplementary figure S5). Using these isotopic end-member values, it seems that the Stomanovo monzonites can be produced by considerably large (50%) assimilation of gneisses by the absarokitic magma.

9.d. Potassium enrichments

Most current models for the origin of mafic U-K and shoshonitic magmas propose derivation from a metasomatised sub-continental lithospheric mantle source. The metasomatic agent is assumed to be derived from subducted sediments or subducted continental crust (e.g., Foley et al. 1987; Conticelli, 1998; Prelević & Foley, 2007; Conticelli et al. 2009; Avanzinelli et al. 2011; Crummy et al. 2014; Zhang et al. 2017). Recycled materials, in forms of fluids and/or melts re-fertilize the refractory lithospheric mantle aiding crystallization of new minerals, possibly accommodated in a vein network or through pervasive metasomatism of peridotites

(Foley, 1992; Conticelli et al. 2009; Tomanikova et al. 2019) or by forming a mantle-crustal mélange (Zhang et al. 2017). Based on experimental data and Sr, Nd, Pb and Hf isotopic evidence, large amounts of mica-bearing lithologies (e.g., glimmerite, phylites, blueschists, terrigenous siliciclastic sediments, marly sediments, among others) have been proposed to have a role in the metasomatic process (Prelević et al. 2008; Avanzinelli et al. 2011; Wang et al. 2017; Foster et al. 2018, 2020).

Although the model of mantle metasomatism via subduction fluids and melts can explain the K-enrichment of the Stomanovo monzonite, they are inconsistent with the large quantity of zircons from the underlying Rhodopean metamorphic basement. It is interesting to point out that apart from the zircons, no other types of xenocrysts have been found. As already mentioned, prevailing rock lithologies comprising the underlying metamorphic basement of the Rhodope metamorphic core complex are biotite, K-feldspar and muscovite-bearing gneisses and two-mica shists (Mposkos & Krohe, 2006; Collings et al. 2016 and references therein). Entrainment, disintegration, disaggregation and dehydration-melting reactions of xenoliths of such composition, which can reach complete fusion at magmatic temperature of ~ 1000°C and greater depth (Reiners et al. 1995; Beard et al. 1993), can explain the lack of xenocryst mineral diversity. Rohrmeier et al. (2013) demonstrated that micas and K-feldspars from the basement metamorphic rock have high $^{87}Sr/^{86}Sr$ ratios and high Rb (up to 1372 ppm in the biotite, 878 ppm in the muscovite and up to 897 ppm in the K feldspar). Therefore, elevated concentrations of Rb and Ba in the monzonite, along with the reported high $^{87}Sr/^{86}Sr$ ratio, can be explained by assimilation of biotite, muscovite and K-feldspar lithologies.

In summary, we propose that assimilation of biotite, K-feldspar, muscovite and other minerals in the underlying metamorphic rocks can increase K, Ba, Rb and LREE concentrations, as well as $^{87}Sr/^{86}Sr$ ratios of an originally lower K magma and reach the values observed in the Stomanovo monzonite. Our small scale focused study supports the modelling results of Beard et al. (2005) that concerns crust-mantle mixing in silicic magmas. Perhaps a combination of age determination of zircon xenocryst populations and petrology and geochemistry of even larger high-K igneous bodies may prove a powerful method to decipher the true origins of such “exotic” and yet very informative magmatic rock varieties.

10. Conclusions

1. Compositional diversity and complex zoning of the CPXs, variable zircon populations and crustal Sr-Nd isotopic signatures indicate a complex origin for the Stomanovo U-K monzonite involving fractional crystallization, crystal-melt mixing and crustal contamination.
2. The elemental and isotopic characteristics of the Stomanovo U-K monzonite can be explained as the result assimilation of K-rich minerals into a calc-alkaline primitive magma. The process is inferred by the high $^{87}Sr/^{86}Sr$ and low $^{143}Nd/^{144}Nd$ isotopic ratios and the abundant presence of zircon xenocrysts. Correspondence of the isotopic compositions and ages of the zircon xenocrysts with the underlying metamorphic basement indicates that the Rhodope metamorphic and igneous basement was the major crustal contaminant.
3. High-Fe CPX cores crystallized in a highly fractionated and probably contaminated magma, whereas high-Mg CPXs crystallized in a primitive mantle-derived mafic magma. Inclusion of the high-Fe CPX into high-Mg CPX, indicates mixing between disrupted evolved cumulate rocks and the primitive magma.
4. Crystallization and crystal-melt mixing occurred at high to moderate pressure, most probably in the lower and middle crust. The final composition was formed by combined fractional crystallization and crustal contamination in the middle and upper crust.

Acknowledgements: We thank Orlando Vaselli for the assistance in microprobe analyses and Fabio Caponi for the XRF analyses. D. Prelević and an anonymous reviewer are thanked for their comments and suggestions that improved the final manuscript. This study was partially supported by Bulgarian Ministry of Education and Sciences National Research Programme "Environmental Protection and Reduction of Risks of Adverse Events and Natural Disasters" approved by DCM # 577/17.08.2018.

References

Abbo, A., Avigad, D. & Gerdes, A. 2020. Crustal evolution of peri-Gondwana crust into present day Europe: The Serbo-Macedonian and Rhodope massifs as a case study, *Lithos* 356-357, 105295.

Avanzinelli, R., Elliott, T., Tommasini, S. & Conticelli, S. 2007. Constraints on the genesis of potassium-rich Italian volcanic rocks from U/Th disequilibrium. *Journal of Petrology* 49, 195–223.

Barton, M. & Van Bergen, M. J. 1981. Green clinopyroxenes and associated phases in a potassium-rich lava from the Leucite Hill, Wyoming. *Contributions to Mineralogy and Petrology* 77, 101-114.

Barton, M., Varekamp, J. C. & Van Bergen, M. J. 1982. Complex zoning of clinopyroxenes in the lavas of Vulsini, Latium, Italy: evidence for magma mixing. *Journal of Volcanology and Geothermal Research* 14, 361-388.

Beard, J. S., Abitz, R. J. & Lofgren, G. E. 1993. Experimental melting of crustal xenoliths from Kilbourne Hole, New Mexico and implications for the contamination and genesis of magmas. *Contributions to Mineralogy and Petrology*, **115**, 88–102.

Beard, J. S., Ragland, P. S. & Crawford, M. L. 2005. Reactive bulk assimilation: A model for crust-mantle mixing in silicic magmas. *Geology*; 33, 681–684;

Boari, E. & Conticelli, S. 2007. Mineralogy and petrology of associated Mg-rich ultrapotassic, shoshonitic, and calc-alkaline rocks: the Middle Latin Valley monogenetic volcanos, Roman Magmati Province, Southern Italy. *Canadian Mineralogist* 45, 1727–1754.

Bonev, N. & Beccaletto, L. 2007. From syn- to post-orogenic Tertiary extension in the north Aegean region: constraints on the kinematics in the eastern Rhodope–Thrace, Bulgaria–Greece and the Biga Peninsula, NW Turkey. In: *The Geodynamics of the Aegean and Anatolia.* (eds T. Taymaz, Y. Yilmaz & Y. Dilek), pp. 113–142. Geological Society, London, Special Publication. no. 291,

Bonev, N., Ovtcharova-Schaltegger, M., Moritz, R., Marchev, P. & Ulianov, A. 2013. Peri-Gondwanan Ordovician crustal fragments in the high-grade basement of the Eastern Rhodope Massif, Bulgaria: evidence from U-Pb LA-ICP-MS zircon geochronology and geochemistry. *Geodinamica acta* 26, 207-229.

Bonev, N., Marchev, P., Moritz, R. & Colling, D. 2015. Jurassic subduction zone tectonics of the RhodopeMassif in the Thrace region (NE Greece) as revealed by new U–Pb and $^{40}Ar/^{39}Ar$ geochronology of the Evros ophiolite. *Gondwana Research* 27, 760-775.

Brooks, C. K.& Printzlau, I. 1978. Magma mixing in mafic alkaline volcanic rocks: The evidence from relict phenocryst phases and other inclusions. *Journal of Volcanology and Geothermal Research* 4,315–331

Burg, J-P., Ivanov, Z., Ricou, L., E. Dimov, D. & Klain, L. 1990. Implications of shear-sense criteria for the tectonic evolution of the Central Rhodope massif, southern Bulgaria. *Geology* 18, 451-454.

Burg, J-P., Ricou, L. E., Ivanov, Z., Godfriaux, I., Dimov, D. & Klain, L.1996. Syn-meta morphic nappe complex in the Rhodope Massif: Structure and kinematics. *Terra Nova* 8, 6–15.

Burg, J-P. 2012. Rhodope: From Mesozoic convergence to Cenozoic extension. Review of petro-structural data in the geochronological frame. Journal of the Virtual Explorer, 2012.Volume 42 paper 1. In: *The Geology of Greece*. (eds E. Skourtos & G.S. Lister). ttp://virtualexplorer.com.au/.

Collings, D., Savov, I. P., Maneiro, K., Baxter, E., Harvey, J. & Dimitrov, I. 2016. Late Cretaceous UHP metamorphism recorded in kyanite-garnet schists from the Central Rhodope Mountains, Bulgaria. *Lithos* 246-247, 165-181.

Conticelli, S. 1998. Effects of crustal contamination on ultrapotassic magmas with lamproitic affinity: mineralogical, geochemical and isotope data from the Torre Alfina lavas and xenoliths, Central Italy. *Chemical Geology* 149, 51-81.

Conticelli, S., Guarnieri, L., Farinelli, A., Mattei, M., Avanzinelli, R., Bianchini, G., Boari, E., Tommasini, S., Tiepolo, M., Prelević, D. & Venturelli, G. 2009. Trace elements and Sr-Nd-Pb isotopes of K-rich, shoshonitic, and calc-alkaline magmatism of the western Mediterranean region: genesis of ultrapotassic to calc-alkaline magmatic associations in a post-collisional geodynamic setting. *Lithos* 107, 68-92.

Crummy, J., Savov, I. P, Navarro-Ochoa, C., Morgan, D. Wilson, M. 2014. High-K mafic Plinian eruptions of Volcán de Colima, México. *Journal of Petrology* 55 (10), 1-18.

Davidson, J. P., Hora, J. M., Garrison, J. M. Dungan, M. A. 2005. Crustal forensics in arc magmas. *Journal of Volcanology and Geothermal Research* 140, 157-170.

DeBari, S. M. Coleman, R. G. 1989. Examination of the deep levels of an island arc: evidence from the Tonsina ultramafic–mafic assemblage, Tonsina, Alaska. *Journal of Geophysical Research* 94, 4373–4391.

Del Moro, A., Innocenti, F., Kyriakopoulos, C., Manetti, P. Papadopoulos, P. 1988. Tertiary granitoids from Thrace (northern Greece): Sr isotopic and petrochemical data. *Neues Jahrbuch für Geologie und Paläontologie Abhandlungen* 159, 113–135.

DePaolo, D. J. 1981. Trace element and isotopic effects of combined wall-rock assimilation and fractional crystallization. *Earth and Planetary Science Letters* 53, 189-202.

DePaolo, D. J., Perry, F. V. & Baldridge, W. S. 1992. Crustal vs. mantle sources of granitic magmas: A two parameter model based on Nd isotopic studies. *Royal Society of Edinburgh Transactions, Earth Sciences* 83, 439–446.

Di Battistini, G., Montanini, A., Vernia, L., Bargossi, D.G. & Gastotina, F. 1999. Petrology and geochemistry of ultrapotassic rocks from the Montefiascone volcanic complex (Central Italy), magmatic evolution and petrogenesis. *Lithos* 43, 169-195.

Dobosi, G. 1989. Clinopyroxene zoning patterns in the young alkali basalts of Hungany and their petrogenetic significance. *Contributions to Mineralogy and Petrology*. 101, 112–121.

Dobosi, G. & Fodor, R. V. 1992. Magma fractionation, replenishment, and mixing as inferred from green-core clinopyroxenes in Pliocene basanite, southern Slovakia. *Lithos* 28, 133-150.

Duda, A. & Schmincke, H. U. 1985. Polybaric differentiation of alkali basaltic magmas: evidence from green-core clinopyroxenes (Eifel, FRG). *Contributions to Mineralogy and Petrology* 91, 340-353.

Fedele, L., Lustrino, M., Melllluso, L., Morra, M., Zanetti, A. & Vannucci. R. 2015. Trace-element partitioning between plagioclase, alkali feldspar, Ti-magnetite, biotite, apatite, and evolved potassic liquids from Campi Flegrei (Southern Italy). *American Mineralogist* 100, 233–249, 2015.

Filipov, P. Marchev, P. Peytcheva, I. von Quadt, A. & Georgiev, S. 2017. Bratsigovo-Dospat volcanic area (Central Rhodopes, Bulgaria) – The link between East and West Rhodope magmatism in late Paleogene: Constraints from Sr-Nd-Hf isotopic studies. Proceedings of XXXIV International Conference. Miass, 4-9 August. 2017, pp. 72-74.

Foley, S. 1992. Vein-plus-wall-rock melting mechanisms in the lithosphere and the origin of potassic alkaline magmas. Original Research Article. *Lithos* 28 435-453.

Foley, S F, Venturelli, G., Green, D.H. & Toscani, L. 1987. The ultrapotassic rocks: characteristics, classification, and constraints for petrogenetic models. *Earth Science Reviews* 24, 81-134.

Förster, M.W., Buhre, S., Xu B., Prelević, Mertz-Kraus, R. & Foley, S F. 2020. Two-Stage Origin of K-Enrichment in Ultrapotassic Magmatism Simulated by Melting of experimentally Metasomatized Mantle. *Minerals* 10, 41.

Förster, M.W., Prelević, D., Buhre, S., Mertz-Kraus, R. & Foley, S.F. 2019.An experimental study of the role of partial melts of sediments versus mantle melts in the sources of potassic magmatism. *Journal of Asian Earth Sciences* 177, 76–88.

Förster, M.W., Prelević, D., Schmück, H.R., Buhre, S., Marschall, H.R., Mertz-Kraus, R. & Jacob, D.E. 2018. Melting phlogopite-rich MARID: amproites and the role of alkalis in olivine-liquid Ni-partitioning. *Chemical Geology* 476, 429–440.

Froitzheim, N., Jahn-Awe, S., Frei, D., Wainwright, A., N Maas, R., Georgiev, N., Nagel, T. J. & Pleuger. J. 2014. Age and composition of meta-ophiolite from the Rhodope Middle Allochthon (Satovcha, Bulgaria): A test for the maximum-allochthony hypothesis of the Hellenides. *Tectonics* 32, 1477-1500 doi:10.1002/2014TC003526.

Gülmez, F., Genc, S. C., Prelević, D., Tüysüz, O., Karacık, Z., Roden, M. F. Z. & Billor, Z. 2016. Ultrapotassic Volcanism from the Waning Stage of the Neotethyan Subduction: A Key Study from the Izmir-Ankara-Erzincan Suture Belt, Central Northern Turkey. *Journal of Petrology* 57, 561–593.

Harkovska, A., Marchev, P., Machev, Ph.& Pecskay, Z. 1998. Paleogene magmatism in the Central Rhodope area, Bulgaria — a review and new data. *Acta Vulcanologica* 10, 199–216.

Harkovska, A. & Velinov, I. 2002. New data about genesis of the secondary quartzites from occurrence "Stomanovo", Central Rhodopes. *Mining and geology* 9, 27-34 (in Bulgarian).

Harkovska, A., Yanev, Y. & Marchev, P. 1989. General features of the Paleogene orogenic magmatism in Bulgaria. *Geologica Balcanica* 19, 37-72.

Hildreth, W. & Moorbath, S. 1988. Crustal contributions to arc magmatism in the Andes of central Chile. *Contributions to Mineralogy and Petrology*. 98, 455–489.

Himmerkus, F., Reischmann, T. & Kostopoulos, D. 2009. Serbo-Macedonian revisited: A Silurian basement terrane from Northern Gondwana in the Internal Hellenides, Greece. *Tectonophysics,* 473, 20–35.

Huang, X. L., Niu, Y. L., Xu, Y. G. Chen, L. L. & Yang, Q.J. 2010. Mineralogical and geochemical constraints on the petrogenesis of post-collisional potassic and ultrapotassic rocks from western Yunnan, SW China. *Journal of Petrology*, 51, 1617−1654.

Jan, M. Q. & Howie, R. A. 1981. The mineralogy and geochemistry of the metamorphosed basic and ultrabasic rocks of tlhe Jijal complex, Kohistan, NW Pakistan. *Journal of Petrology*. 22, 85-126.

Janák, M., Froitzheim, N., Georgiev, N., Nagel, T. J. & Sarov. S. 2011. P-T evolution of kyanite eclogite from the Pirin Mountains (SW Bulgaria): implications for the Rhodope UHP Metamorphic Complex. *Journal of Metamorphic Geology* 29,317–332.

Jankovics, M., É. Dobosi, G., Embey-Isztin, A., Kiss, B., Sági, T., Harangi, S. & Ntaflos, T. 2013. Origin and ascent history of unusually crystal-rich alkaline basaltic magmas from the western Pannonian Basin. *Bulletin of Volcanology* 75,749 DOI 10.1007/s00445-013-0749-7

Jones, C., E., Tarney, J., Baker, J. H. & Gerouki, F. 1992. Tertiary granitoids of Rhodope, northern Greece: Magmatism related to extensional collapse of the Hellenic Orogen?, *Tectonophysics*, 210(3–4), 295–314, doi:10.1016/0040-1951(92)90327-3.

Kackov, N. 1987. Reconstruction des Paleovulkanismus im Bracigovo-Dospater Vilkanitmassiv (Bulgarien). *Zeitschrift für Angewandte Geologie.* 33, 175-179.

Kamenov, B., Peytcheva, I., Klain, L., Arsova, K., Kostitsin, Y.& Salnikova, E. 1999. Rila-West Rhodopes Batholith: Petrological and geochemical constraints for its composite character. *Geochimistry Mineralogy and Petrology* 36, 3-27.

Katskov, N. 1980. Structure of a part of the Bratsigovo-Dospat effusion. *Geotectonics, tectonophysics and geodynamics* 11, 3-24

Kilias, A., Falalakis, G. & Mountrakis, D. 1999. Cretaceous–Tertiary structures and kinematics of the Serbomacedonian metamorphic rocks and their relation to the exhumation of the Hellenic hinterland (Macedonia, Greece). *International Journal of Earth Sciences* 88, 513-531.

Kirchenbaur, M., Münker, C., Schuth, S., Garbe-Schönberg, D. & Marchev, P. 2012a. Tectonomagmatic constraints on the sources of Eastern Mediterranean K-rich lavas. *Journal of Petrology* 53, 1, 27-65.

Kirchenbaur, M., Pleuger, J. Jahn-Awe, S., Nagel, T. J., Froitzheim, N., Fonseca, R. O. C. & Munker, K. 2012b. Timing of high-pressure metamorphic events in the Bulgarian Rhodopes from Lu–Hf garnet geochronology. *Contributions to Mineralogy and Petrology* 163, 97-921.

Koglin, N., Reischmann, T., Kostopoulos, D., Matukov, D. & Sergeev, S. 2007. Zircon SHRIMP ages and the origin of ophiolitic rocks from the NE Aegean region, Greece. *Geophysical Research Abstracts* 9 (paper 06848).

Kolokotroni, C. N. & Dixon, J. E. 1991. The origin and emplacement of the Vrondou granite, Serres, NE Greece. *Bulletin of the Geological Society of Greece* 25, 469–483.

Koukouvelas, I. & Doutsos, T. 1990. Tectonic stages along a traverse cross cutting the Rhodopian zone (Greece). *Geologische Rundschau* 79, 753–776.

Krenn, K., Bauer,C., Proyer, A, Klötzli, U. & Hoinkes, G. 2010. Tectonometamorphic evolution of the Rhodope orogen, *Tectonics* 29, TC4001, doi:10.1029/2009TC002513

Krohe, A. & Mposkos, E. 2002. Multiple generations of extensional detachments in the Rhodope Mountains (northern Greece): evidence of episodic exhumation of high-pressure rocks. In *The Timing and Location of Major Ore Deposits in an Evolving Orogen* (eds D. J. Blundell, F. Neubauer & A. von Quadt), pp.151-178. Geological Society, London, Special Publications no 204,.

Liati, A. Gebauer, D. & Fanning, C. M. 2011. Gechronology of the Alpine UHP Rhodope Zone: a review of isotopic ages and constraints on the geodynamic evolution. In: *Ultrahigh-pressure Metamorphism. 25 years after the discovery of coesite and diamond* (eds L. F. Dobrzhinetskaya, S.W. Faryad, S. Wallis & Cuthbert, S), pp. 295–324. Elsevier.

Macheva, L., Peytcheva, I., von Quadt, A., Zidarov, N. & Tarassova, E. 2006. Petrological, geochemical and isotope features of Lozen metagranite, Belasitza Mountain-evidence for widespread distribution of Ordovician metagranitoids in the Serbo-Macedonian Massif, SW Bulgaria. In: National Conference "Geosciences 2006", proceedings, Sofia 2006, pp 209–212

Marchev, P., Arai, S., Ishida, Y., Shirasaka, M., Downes, H. 2008. Trace element and isotopic composition of mafic and ultramafic cumulate xenoliths in alkaline basalts from the Eastern Rhodopes, Bulgaria: Inferences on deep processes under the metamorphic core complexes. *IOP Conference Series: Earth and Environmental Science*, 2, 012015

Marchev, P., Arai, S. & Vaselli, O. 2006. Cumulate xenoliths series in the Krumovgrad alkaline basaltic and lamprophyric dykes: Evidence for the existence of layered plutons under the Eastern Rhodope metamorphic core-complexes, Bulgaria. In *Post-collisional Tectonics and magmatism in the Eastern Mediterranean Region* (eds Y. Dilek, Y & S. Pavlides), pp. 237-258. Geological Society of America Special Papers no 409.

Marchev. P. & Filipov, P. 2012. First findings of Late Cretaceous magmatic rocks in the Pirin Mts. Bulgarian Geological Society, National conference, *Geosciences 2012, Proceedings*, pp. 55–56.

Marchev, P., Raicheva, R., Downes, H.,Vaselli, O., Chiaradia, M. & Moritz, R. 2004. Compositional diversity of Eocene-Oligocene basaltic magmatism in the Eastern Rhodopes, SE Bulgaria: implications for genesis and tectonic setting. *Tectonophysics* 393, 301-328.

Marchev, P., Rogers, G., Conrey, R., Quick, J., Vaselli, O. & Raicheva, R. 1998. Paleogene orogenic and alkaline basic magmas in the Rhodope zone: relationships, nature of magma sources, and role of crustal contamination. *Acta Vulcanologica* 10 (2), 217–232.

Marchev, P., Georgiev S., Raicheva R., Peytcheva I., A. von Quadt, Ovtcharova M., & Bonev N. 2013. Adakitic magmatism in postcollisional setting: An example from the early-middle Eocene magmatic belt in southern Bulgaria and northern Greece. *Lithos* 180-181, 159-180. DOI:10.1016/j.lithos.2013.08.024.

Marchev, P., Von Quadt, A., Peytcheva, I. & Ovtcharova, M. 2006. The age and origin of the Chuchuliga and Rozino granites, Eastern Rhodopes. Bulgarian Geological Society, National conference, *Geosciences* 2006. Proceedings, pp. 213–216.

Mavroudchiev, B., Nedyalkov, R., Eleftheriadis, G., Soldatos, T. & Christofides, G. 1993. Tertiary plutonic rocks from east Rhodope in Bulgaria and Greece. *Bulletin of the Geological Society of Greece* 28, 643– 660.

Middlemost, E. 1994. Naming materials in the magma/igneous rock system. *Earth-Science Reviews* 37, 215–224.

Miladinova, I., Froitzheim, N., Nagel, T. J., Janák, M., Georgiev, N., Fonseca, R. O. C., Sandmann, S. & Münker, C. 2018. Late Cretaceous eclogite in the Eastern Rhodopes (Bulgaria): evidence for subduction under the Sredna Gora magmatic arc. *International Journal of Earth Sciences* 107, 2083–2099.

McLeod, C, L., Davidson, J. P., Nowell, G. M. & de Silva, S. L. 2012. Disequilibrium melting during crustal anatexis and implications for modeling open magmatic systems. *Geology* 40 (5), 435-438.

Morimoto, N., Fabries, J., Ferguson, A. K., Ginzburg, I. V., Ross, M., Seifert, F. A., Zussman, J., Aoki, K. & Gottardi, G. 1989. Nomenclature of pyroxenes. Subcommittee on pyroxenes. *American Mineralogist* 73, 1123–1133.

Mposkos, E.& Krohe, A. 2006. Pressure–temperature-deformation paths of closely associated ultra-high-pressure (diamond-bearing) crustal and mantle rocks of the Kimi complex: implications for the tectonic history of the Rhodope Mountains, Northern Greece. *Canadian Journal of Earth Sciences* 43, 1755–1776.

Müntener, O., Kelemen, P. B. & Grove,T. L. 2001. The role of H_2O during crystallization of primitive arc magmas under uppermost mantle conditions and genesis of igneous pyroxenites: an experimental study. *Contributions to Mineralogy and Petrology* 141, 643-658.

Papanikolaou, D. 2009. Timing of tectonic emplacement of the ophiolites and terrane paleogeography in the Hellenides. *Lithos* 108, 262–280.

Peccerillo, A. & Martinotti, G. 2006. The Western Mediterranean lamproitic magmatism: origin and geodynamic significance. *Terra Nova* 18, 109-117.

Peccerillo, A. & Taylor, S.R. 1976. Geochemistry of Eocene calc-alkaline volcanic rocks from the Kastamonu area, northern Turkey. *Contributions to Mineralogy and Petrology* 58, 63-81.

Peytcheva, I., Kostitsin, Y. Salnikova, E., Kamenov, B. & Klain, L. 1998. Rb–Sr and U–Pb isotope data for the Rila–Rhodopes batholith. *Geochemistry Mineralogy and Petrology* 35, 93–105. (in Bulgarian with English abstract).

Peytcheva, I. & von Quadt, A. 1995. U-Pb zircon dating of metagranites of Byala-Reka region in the East Rhodopes of Bulgaria. Proc. XV Congress of CBGA, *Geological Society of Greece, Special Publication*, 4, 627-631.

Peytcheva, I., von Quadt, A., Ovtcharova, M., Handler, R., Neubauer, F., Salnikova, E., Kostitsyn, Yu., Sarov, S. & Kolcheva, K. 2004. Metgranitoids from the eastern part of the Central Rhodopean Dome (Bulgaria): U–Pb, Rb–Sr and 40Ar/39Ar timing of emplacement and exhumation and isotope-geochemical features. *Mineralogy and Petrology* 82, 1–31.

Peytcheva, I., von Quadt, A., Sarov, S., Voinova, E. & Kolcheva, K. 2009. Ordovician protoliths of metamorphic rocks in Eastern Pirin– Western Rhodopes—are they part of the Ograzhden Unit? In: National Conference "*Geosciences 2009*", proceedings, Sofia 2009, pp 17–18

Prelević, D., Akal, C., Foley, S. F., Romer, R., Stracke, A. & van den Bogaard, P. 2012. Ultrapotassic Mafic Rocks as Geochemical Proxies for Post-collisional Dynamics of Orogenic Lithospheric Mantle: the Case of Southwestern Anatolia, Turkey. *Journal of Petrology* 53, 1019-1055.

Prelević, D., Akal, C., Romer, R. L., Mertz-Kraus, R. & Helvaci, C. 2015. Magmatic Response to Slab Tearing: Constraints from the Afyon Alkaline Volcanic Complex, Western Turkey. *Journal of Petrology*, 56(3), 527–562.

Prelević, D. & Foley, S. F. 2007. Accretion of arc-oceanic lithospheric mantle in the Mediterranean: evidence from extremely high-Mg olivines and Cr-rich spinel inclusions in lamproites. *Earth and Planetary Science Leters* 256, 120-135.

Prelević, D., Foley, S. F., Romer, R. & Conticelli, S. 2008. Mediterranean Tertiary lamproites derived from multiple source components in postcollisional geodynamics. *Geochimica et Cosmochimica Acta* 72, 2125–2156.

Putirka, K. 2008. Thermometers and barometers for volcanic systems. In *Minerals, Inclusions and Volcanic Processes* (eds Putirka, K. & Tepley, F.), pp. 61–120. Reviews in Mineralogy and Geochemistry 69. Mineralogical Society of America.

Reiners, P.W., Nelson, B. K. & Ghiorso, M. S. 1995. Assimilation of felsic crust by basaltic magma: Thermal limits and extents of crustal contamination of mantle-derived magmas. *Geology* 23, 563–566.

Rohrmeier, M. K., Von Quadt, A., Dreisner, T., Heinrich, C. A., Handler, R., Ovtcharova, M., Ivanov, Z., Petrov, P.,Sarov, St. & Peytcheva, I. 2013. Post-Orogenic Extension and Hydrothermal Ore Formation:High-Precision Geochronology of the Central Rhodopian etamorphic Core Complex (Bulgaria-Greece). *Economic Geology* 108, 691–718.

Rudnick, R. L. & Gao, S. 2003. Composition of the continental crust. In *The Crust* (ed. Rudnick, R. L.), pp. 1–64. Oxford: Elsevier-Pergamon, Treatise on Geochemistry, no. 3.

Sarov, S., Naydenov, K., Zhelezarski, T., Marinova, R., Georgieva, I., Ivanova, D., Popov, A., Markov, N. 2009. *Geological map of the Republic of Bulgaria in scale 1:50 000, K-35-73-G (Devin) map sheet.* Ministry of Environment and Waters, Bulgarian National Geological Survey, Sofia.

Shaw, C. S. J. & Eyzaguirre, J. 2000. Origin of megacrysts in the mafic alkaline lavas of the West Eifel volcanic field, Germany. *Lithos* 50, 75–95.

Sokol, K. Halama, R., Meliksetian, K., Savov, I. P. & Sudo, M. 2018. Alkaline magmas in zones of continental convergence: The Tezhsar volcano-intrusive ring complex, Armenia, *Lithos* 321, 172-19

Soldatos, T., Koroneos, A., Kamenov, B., Peytcheva, I., von Quadt, A., Christofides, G., Zheng, X. & Sang, H. 2008. New U–Pb and Ar–Ar mineral ages for the Barutin–Buynovo–Elatia–Skaloti–Paranesti batolith (Bulgaria and Greece): refinement of its debatable age. *Geochemistry Mineralogy and Petrography* 46, 85–102.

Sun, S-S. & McDonough, W. F. 1989. Chemical and isotopic systematics of oceanic basalts: implications for mantle composition and processes. In *Magmatism in the Ocean Basins* (eds A. D. Saunders & M. J. Norry). Pp.313-345. Geological Society of London, Special Publication no 42,

Tomanikova, L., Savov, I. P., Harvey, J., DeHoog, C-J., Churikova, T., Gordeichyk, B. & Yogodzinsky, G. 2019. Boron and B isotope systematics of metasomatised mantle xenoliths from the Kamchatka arc. *Geology* 47, 517-521.

Turpaud, P. & Reischmann, T. 2010. Characterisation of igneous terranes by zircon dating: Implications for UHP occurrences and suture identification in the Central Rhodope, northern Greece. *International Journal of Earth Sciences* 99, 567–591, doi:10.1007/s00531-008-0409-x.

Varekamp, J. C. & Kalamarides, R. I. 1989. Hybridization processes in leucite tephrite from Vulsini, Italy, and the evolution of the Italian potassic suite. *Journal of Geophysical Research* 94, 4603-4618.

Velinov, I., Kunov, A. & Velinova, N. 2007. *The metasomatic secondary quartzite formation in Bulgaria*. Prof. Marin Drinov Academic Publishing House, Sofia.198 pp.

von Quadt, A. & Peytcheva, I. 2005. The southern extension of the Srednogorie type Upper Cretaceous magmatism in Rila–Western Rhodopes: constraints from isotope geochronological and geochemical data. Bulgarian Geological Society 80th anniversary, Proceedings, pp. 113–116.

von Quadt, A. Peytcheva, I. Sarov, S. & Naydenov, K. 2008. Metamorphic rocks from Dospat area of western Rhodopes—conventional and in situ U-Pb zircon dating, isotope tracing and correlations. "*GEOSCIENCES 2008*", 33-34.

von Quadt, A. & Peytcheva, I. 2005. The southern extension of the Srednogorie type Upper Cretaceous magmatism in Rila–Western Rhodopes: constraints from isotope geochronological and geochemical data. Bulgarian Geological Society 80th anniversary, Proceedings, pp. 113–116.

Wang, Y., Foley, S.F. & Prelević, D. 2017. Potassium-rich magmatism from a phlogopite-free source. *Geology* 45 (5), 467–470.

Wass, S. Y. 1979. Multiple origins of clinopyroxenes in alkali basaltic rocks *Lithos* 12, 115-132.

Wood, B. J. & Blundy, J. D. 2001. A predictive model for rare earth element partitioning between pyroxene and anhydrous silicate melt. *Contributions to Mineralogy and Petrology*. l129, 166-181.

Xu, Y. G., Huang, X. L., Menzies, M. A. & Wang, R. C. 2003. Highly magnesian olivines and green-core clinopyroxenes in ultrapotassic lavas from westernYunnan, China: evidence for a complex hybrid origin. *European Journal of Mineralogy* 15, 965-975.

Yanev, Y. 2003. Mantle source of the Paleogene collision-related magmas of the Eastern Rhodopes (Bulgaria) and Western Thrace (Greece): Characteristics of the mafic magmatic rocks. *Neues Jahrbuch fur Minereralogy Abhanlungen* 178 (2), 131-151.

Yanev, Y., Innocenti, F., Manetti, P & Serri, G. 1998. Upper Eocene–Oligocene collision-related volcanism in eastern Rhodopes (Bulgaria)–Western Thrace (Greece):Petrogenetic Affinity and Geodynamic Significance. *Acta Vulcanol*ogica 10, 265–277.

Yanev, Y. & Ivanova, R. 2009. Paleogene ultrapotassic volcanic rocks of the Eastern Rhodopes, South Bulgaria: Petrology, mineralogy and origin. *Acta Vulcanol*ogica 99-122.

Zagorchev, I., Balica, C., Kozhoukharova, E. & Balintoni, I. C. 2017. Pirin metamorphic and igneous evolution revisited in a geochronological frame based on U-Pb zircon studies. *Geologica Balcanica* 46 (1), 27-63.

Zhang, L, Guo, Z., Zhang, M., Cheng, Z. & Sun, Y. 2017. Post-collisional potassic magmatism in the eastern Lhasa terrane, South Tibet: Products of partial melting of mélanges in a continental subduction channel. *Gondwana Research* 41, 9–28.

Zhu, Y. & Ogasawara Y. 2004. Clinopyroxene phenocrysts (with green salite cores) in trachybasalts: implications for two magma chambers under the Kokchetav UHP massif, North Kazakhstan. *Journal of Asian Earth Sciences* 22, 517–527.

Table 1. Representative chemical analyses and structural formula (O = 6) of pyroxenes from the Stomanovo U-K monzonite

Sample	SV010-83			SV10-128						
	reversely zoned			normally zoned			reversely zoned			
	green core	mantle of green core	rim	core	inner rim	outer rim	green core	outer green core	mantle of green core	rim
SiO_2	50.92	53.48	53.56	53.24	52.47	51.95	52.29	49.38	52.00	52.48
TiO_2	0.60	0.20	0.15	0.29	0.23	0.26	0.29	0.80	0.42	0.38
Al_2O_3	3.29	1.08	0.90	1.85	1.54	0.84	1.07	3.16	2.52	0.94
Cr_2O_3	0.00	0.00	0.01	0.16	0.00	0.00	0.00	0.00	0.01	0.04
FeO	10.38	4.98	6.91	3.73	7.86	9.15	9.97	15.30	4.43	9.27
MnO	0.44	0.19	0.45	0.09	0.29	0.54	0.45	0.32	0.20	0.50
MgO	14.34	17.47	15.92	17.54	15.65	14.68	13.65	10.50	16.44	14.80
CaO	21.13	22.60	22.74	23.55	22.87	21.90	22.02	19.79	24.52	21.70
Na_2O	0.44	0.09	0.32	0.08	0.46	0.30	0.23	0.57	0.16	0.23
K_2O	0.00	0.00	0.03	0.00	0.00	0.07	0.00	0.03	0.00	0.03
P_2O_5										
Total	101.56	100.14	100.99	100.57	101.09	99.69	100.29	99.85	100.70	100.37
Mg#	71.1	86.2	80.4	89.3	78.0	74.1	70.9	55.0	86.9	74.0
Wo	42.7	44.4	44.9	46.2	44.8	43.9	44.8	42.5	48.1	43.5
En	40.3	47.7	43.7	47.9	42.7	40.9	38.6	31.4	44.8	41.2
Fs	17.1	7.9	11.4	5.9	12.5	15.2	16.6	26.2	7.1	15.3
cations										
Si	1.866	1.951	1.954	1.927	1.908	1.939	1.957	1.886	1.886	1.947
Ti	0.017	0.005	0.004	0.008	0.006	0.007	0.008	0.023	0.011	0.011
Al(IV)	0.134	0.046	0.039	0.073	0.066	0.037	0.043	0.114	0.108	0.041
Al(VI)	0.008			0.006			0.004	0.028		
Cr	0.000	0.000	0.000	0.005	0.000	0.000	0.000	0.000	0.000	0.001
Fe3	0.125	0.047	0.067	0.052	0.138	0.092	0.039	0.082	0.107	0.060
Fe2	0.193	0.104	0.144	0.061	0.101	0.193	0.273	0.407	0.027	0.228
Mn	0.014	0.006	0.014	0.003	0.009	0.017	0.014	0.010	0.006	0.016
Mg	0.783	0.950	0.866	0.947	0.848	0.817	0.762	0.598	0.889	0.818
Ca	0.829	0.883	0.889	0.913	0.891	0.876	0.883	0.810	0.953	0.862
Na	0.031	0.006	0.023	0.006	0.032	0.022	0.017	0.042	0.011	0.017

Table 2. Representative trace element (LA-ICP-MS) concentrations of clinopyroxene in the Stomanovo U-K monzonite

Sample	SV010-83		SV10-128								
	normally zoned				reversely zoned						in Sa
Grain#	cpx1		cpx2		cpx3			cpx4		cpx5	cpx6
	core	rim	core	core	green core	green core	mantle of green core	green core	green core	mantle of green core	
Sc	72	135	88	83	40	46	118	51	59	87	168
V	94	143	114	82	326	333	147	270	264	178	251
Cr	715	17	3864	3000	35	118	1253	24	34	25	25
Co	36	37	29	31	48	47	32	40	40	43	34
Ni	147	20	116	130	29	39	123	20	27	95	14
Rb	<0.12	0.56	0.81	0.78	5.37	6.51	4.43	0.56	0.38	<0.50	11.25
Sr	69	50	77	62	61	76	94	5.99	6.75	104	57
Y	8.5	46.5	12.3	6.2	22.5	28.0	8.7	32.6	36.2	14.7	57.7
Zr	9.86	54	10.10	4.14	125	136	22	109	108	33	49
Nb	<0.07	0.14	<0.04	<0.03	0.66	0.55	<0.06	0.43	0.33	<0.16	0.61
Cs	<0.05	<0.04	0.22	0.09	0.67	0.50	0.41	n.d.	n.d.	n.d.	0.90
Ba	0.40	1.79	2.70	0.59	2.87	6.27	1.65	<1.16	1.91	<1.09	35.64
La	1.87	8.32	2.92	1.29	9.27	25.44	2.35	9.81	10.34	4.27	11.06
Ce	7.01	35.73	10.65	4.91	33.99	69.55	9.29	36.01	37.75	14.89	43.61
Pr	1.36	6.20	2.02	0.99	5.29	9.25	1.76	5.99	6.75	2.72	7.74
Nd	9.33	35.94	10.24	5.47	26.03	47.62	10.77	33.07	34.11	13.83	41.86
Sm	2.38	13.67	3.62	2.26	7.13	11.65	3.51	9.28	10.60	4.50	13.34
Eu	0.60	2.22	0.68	0.57	1.31	1.66	0.77	1.51	1.73	1.27	2.07
Gd	3.02	10.65	3.14	1.64	5.67	8.22	3.52	8.89	9.37	5.08	13.16
Tb	0.45	1.59	0.44	0.20	0.82	1.19	0.34	1.23	1.27	0.66	2.07
Dy	1.52	10.08	2.29	1.24	4.08	5.47	2.08	6.53	6.78	2.95	12.46
Ho	0.28	1.83	0.45	0.23	0.81	1.00	0.34	1.16	1.24	0.53	1.99
Er	0.70	5.05	1.06	0.73	1.60	2.26	0.66	3.05	3.36	1.52	5.79
Tm	0.13	0.66	0.15	0.05	0.32	0.35	0.11	0.45	0.51	0.19	0.85
Yb	0.68	4.90	1.34	0.40	2.49	2.98	0.75	3.38	3.52	1.10	5.38
Lu	<0.05	0.62	0.12	0.06	0.37	0.53	0.10	0.58	0.55	0.17	0.88
Hf	0.51	2.26	0.52	0.30	4.97	5.27	1.15	5.10	4.61	1.72	2.03
Ta	<0.07	0.05	<0.03	<0.02	<0.06	<0.05	0.04	0.07	<0.06	<0.16	0.08
Pb	0.51	3.36	4.29	1.80	3.52	5.45	1.24	2.43	4.59	0.86	8.88
Th	<0.06	0.35	0.11	0.05	0.53	5.51	0.31	0.34	0.56	0.61	0.97
U	<0.04	0.10	0.04	<0.02	0.43	1.23	0.09	<0.08	0.10	0.14	0.26

Table 3. Major and trace element analyses of the Stomanovo U-K monzonite.

Sample	SV010-62	SV010-83	SV010-128
SiO_2	58.71	58.96	56.11
TiO_2	0.61	0.61	0.71
Al_2O_3	15.13	15.33	14.70
Fe_2O_3	5.52	6.09	6.98
MnO	0.13	0.16	0.14
MgO	3.18	3.89	4.26
CaO	3.62	3.24	6.73
Na_2O	2.25	2.14	2.21
K_2O	6.05	6.21	5.69
P_2O_5	0.53	0.54	0.66
LOI	2.34	1.88	0.75
Total	98.08	99.06	98.95
Mg#	53.3	55.9	54.7
Sc	8	9	4
V	143	135	165
Cr	48	40	48
Co	14	11	19
Ni	19	14	21
Zn	75	51	71
Cu	30	29	44
Pb	56	49	72
Ga	17	18	
Zr	179	190	169
Hf	6	5.06	4.15
Nb	16	17.52	16.1
Ta		2.60	4.77
U	8	8.27	6.49
Y	31	22.79	24
Th	20	27.48	23.71
Rb	450	447	394
Cs		8.73	10.22
Sr	506	537	714
Ba	2119	2512	3002
La	44	38.89	38.10
Ce	88	77.68	81.04
Pr		9.04	9.76
Nd	37	36.69	40.56
Sm		7.58	8.13
Eu		1.59	2.06
Gd		6.05	6.88
Tb		0.71	0.81
Dy		3.89	4.31
Ho		0.78	0.77
Er		2.27	2.37
Tm		0.28	0.33
Yb		1.96	1.76
Lu		0.21	0.36

Table 4. Sr and Nd isotopic composition of the Stomanovo monzonite

Sample	Rb	Sr	$^{87}Rb/^{86}Sr$	$^{87}Sr/^{86}Sr \pm 2s$	$(^{87}Sr/^{86}Sr)_i$	Nd	Sm	$^{147}Sm/^{144}Nd$	$^{143}Nd/^{144}Nd \pm 2s$	$(^{143}Nd/^{144}Nd)_i$	e^t_{CHUR}
SV010-128	394	714	1.599	0.711351±12	0.710658	40.56	8.13	0.121	0.512225 ± 10	0.512201	-7.8
SV010-128*						40.56	8.13	0.121	0.512213 ± 08	0.512189	-8.0

*replicate

Figure caption:

Fig. 1. (Colour online) (a) Location of the Rhodope and Serbo-Macedonian Massifs in the structural system of the Alpine region in the Balkan Peninsula and western Turkey; (b) Geological map of the Central Rhodopes; (c) Geology of the Stomanovo area after geological map of Bulgaria, M 1: 50 000 (Sarov et al. 2009).

Fig. 2. (Colour online) Cathodoluminescence images showing the range of textures and ages observed in zircons from Stomanovo monzonite porphyry, sample SV10-129: (a) grain c09- prismatic oscillatory zoned crystal; (b) grain a10- rounded crystal with resorbed core, followed by oscillatory outer rim; (c) grain a13- rounded crystal with corroded planar core, followed by oscillatory zone resorbed by light outer rim; (d) grain c15-embayed oscillatory zoned crystal; (e) grain a06- planar xenocrysts (642 Ma) with thin light rim;(f) grain a15- xenocryst with older (747 Ma) corroded core and younger (466 Ma) oscillatory rim. Circles: location of LA-ICP-MS U-Pb analyses. Ages for LA-ICP-MS analyses in Ma.

Fig. 3. (Colour online) Zircon U-Pb concordia diagrams: (a) for the Stomanovo monzonite; (b) for the host ignimbrite

Fig. 4. (Colour online) Clinopyroxenes from the Stomanovo monzonite plotted in conventional Ca-Mg-Fe+Mn diagram (Morimoto et al. 1989).

Fig. 5. (Colour online) Microphotographs showing zoning types of clinopyroxenes and plagioclase. (a) Normally zoned clinopyroxene with Mg-rich core and lower Mg rim; the lowest value is measured in the very thin rim. (b) Reversely zoned clinopyroxene with Fe-rich green core and Mg-rich rim. (c) Normally zoned plagioclase. (d) Sieve-textured plagioclase.

Fig. 6. (Colour online) Chondrite-normalized REE patterns (left panel) and primitive mantle-normalized multi-element patterns (right panel) for clinopyroxene (a, b), feldspars (c, d) and biotite (e, f). Chondrite and PM normalization values are from Sun & McDonough (1989).

Fg. 7. Classification diagrams of the Stomanovo intrusion. (a) K_2O vs. SiO_2 classification diagram after Peccerillo and Taylor (1976). (b) Total Alkali vs.SiO_2 (TAS) diagram (Middlemost, 1994).

Fig. 8. (Colour online) Chondrite-normalized REE patterns: (8a) and primitive mantle-normalized multi-element patterns, (8b) for bulk rocks of the Stomanovo monzonite porphyry. Normalizing values are from Sun & McDonough (1989). Average composition of OIB (Sun & McDonough, 1989) and upper and lower continental crust (Rudnick & Gao, 2003) are given for comparison.

Fig.9. (Colour online) Sr and Nd isotopic compositions of the monzonite, compared with those of the host ignimbrites. Data for the Bratsigovo-Dospat ignimbrite are from Filipov et al. (2017).

Supplementary table S1. Results of Laser Ablation Inductively Coupled Plasma Mass Spectrometry measurements of zircon

Supplementary table S2. Representative major element composition and structural formula (O=8) of feldspar from the Stomanovo U-K monzonite

Supplementary table S3. Representative major element composition and structural formula (O=22) of biotite and ilmenite from the Stomanovo U-K monzonite

Supplementary table S4 Representative trace element (LA-ICP-MS) concentrations of feldspars and phlogopite in the the Stomanovo U-K monzonite

Supplementary figure S5. Assimilation and fractional crystallization (AFC) models

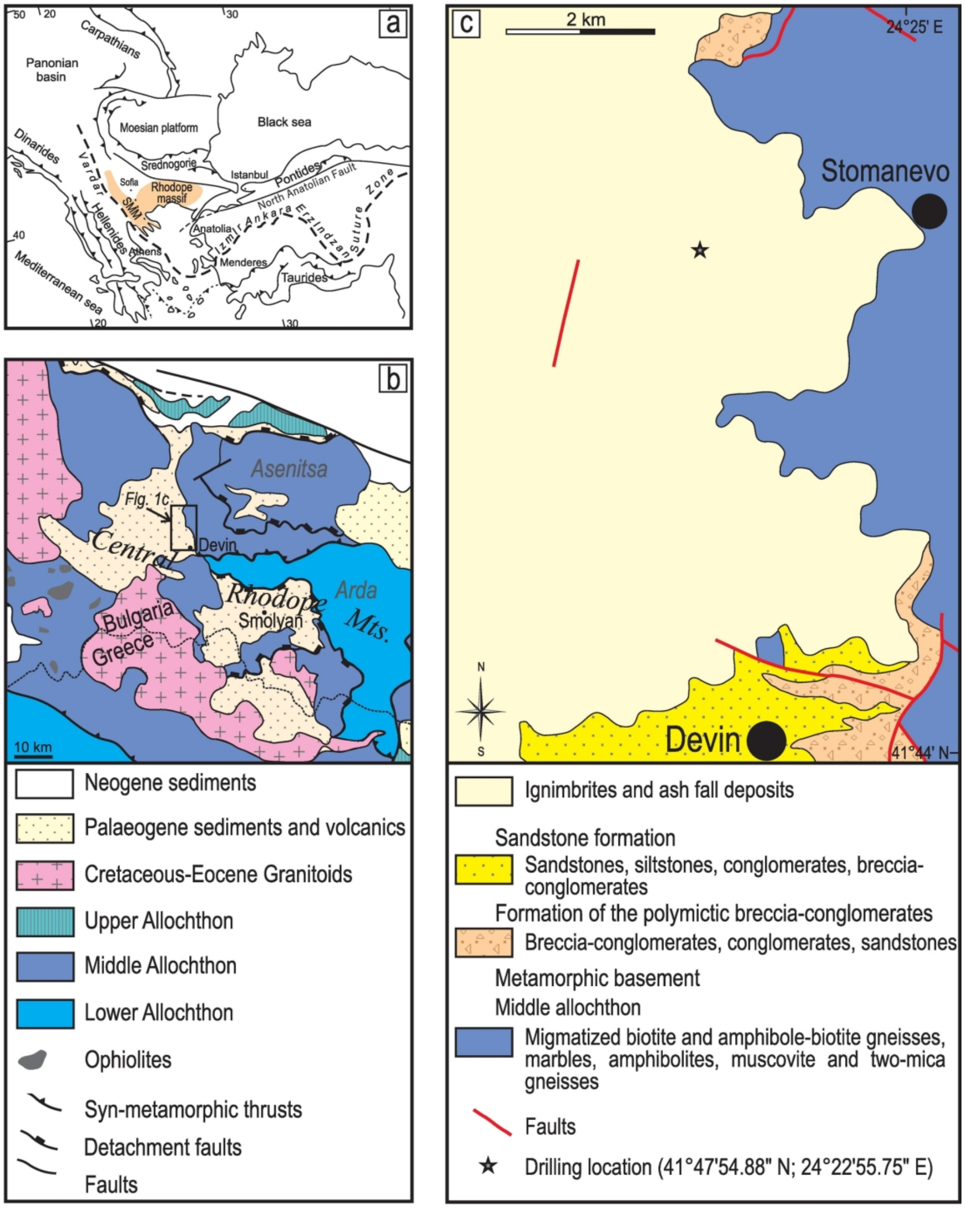

Fig. 1. (Colour online) (a) Location of the Rhodope and Serbo-Macedonian Massifs in the structural system of the Alpine region in the Balkan Peninsula and western Turkey; (b) Geological map of the Central Rhodopes; (c) Geology of the Stomanevo area after geological map of Bulgaria, M 1: 50 000 (Sarov et al. 2009).

169x212mm (300 x 300 DPI)

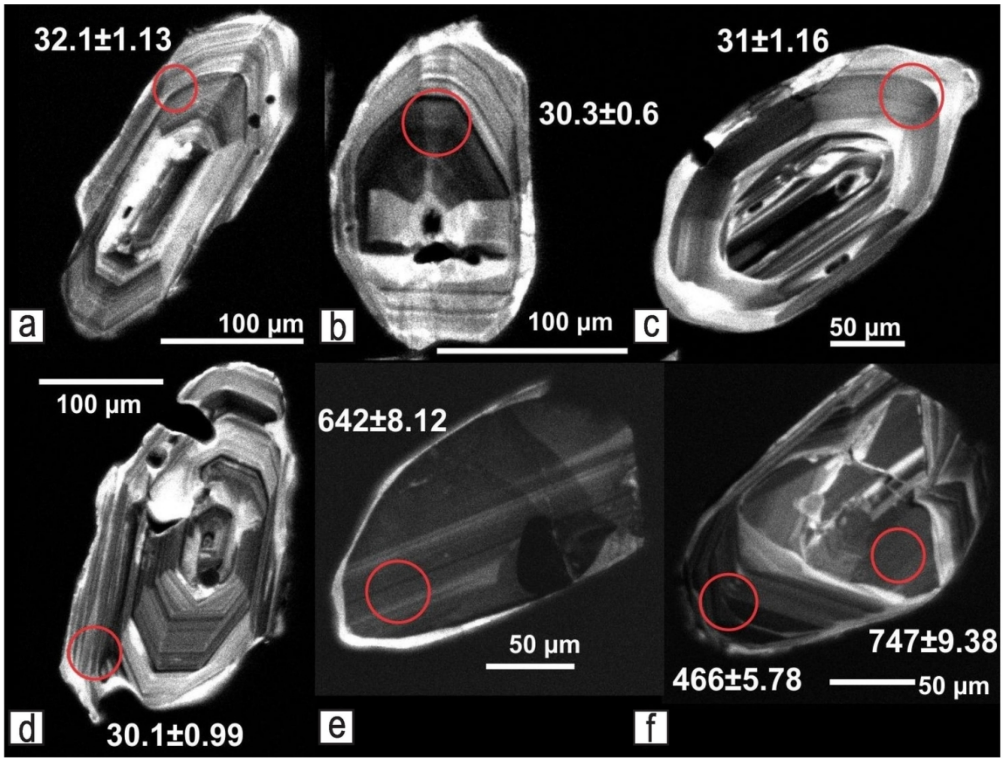

Fig. 2. (Colour online) Cathodoluminescence images showing the range of textures and ages observed in zircons from Stomanovo monzonite porphyry, sample SV10-129: (a) grain c09-prismatic oscillatory zoned crystal; (b) grain a10- rounded crystal with resorbed core, followed by oscillatory outer rim; (c) grain a13- rounded crystal with corroded planar core, followed by oscillatory zone resorbed by light outer rim; (d) grain c15-embayed oscillatory zoned crystal; (e) grain a06- planar xenocrysts (642 Ma) with thin light rim;(f) grain a15- xenocryst with older (747 Ma) corroded core and younger (466 Ma) oscillatory rim. Circles: location of LA-ICP-MS U-Pb analyses. Ages for LA-ICP-MS analyses in Ma.

124x94mm (300 x 300 DPI)

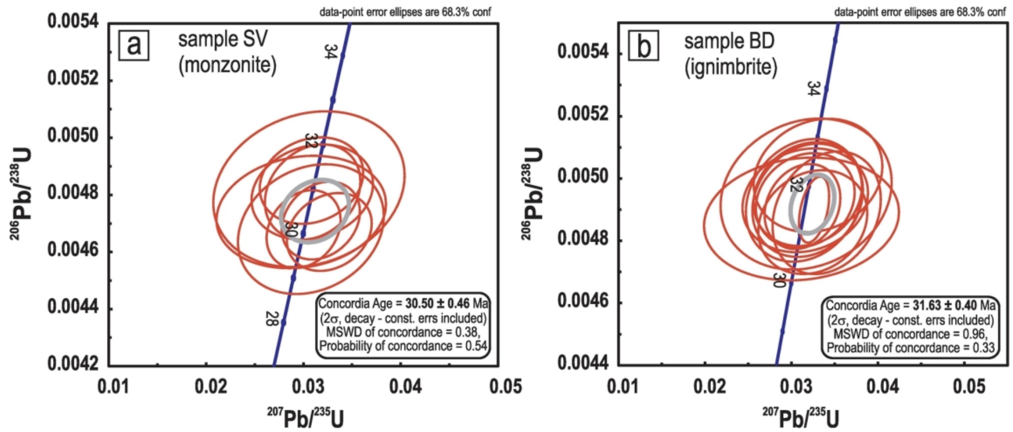

Fig. 3. (Colour online) Zircon U-Pb concordia diagrams: (a) for the Stomanovo monzonite; (b) for the host ignimbrite

170x71mm (300 x 300 DPI)

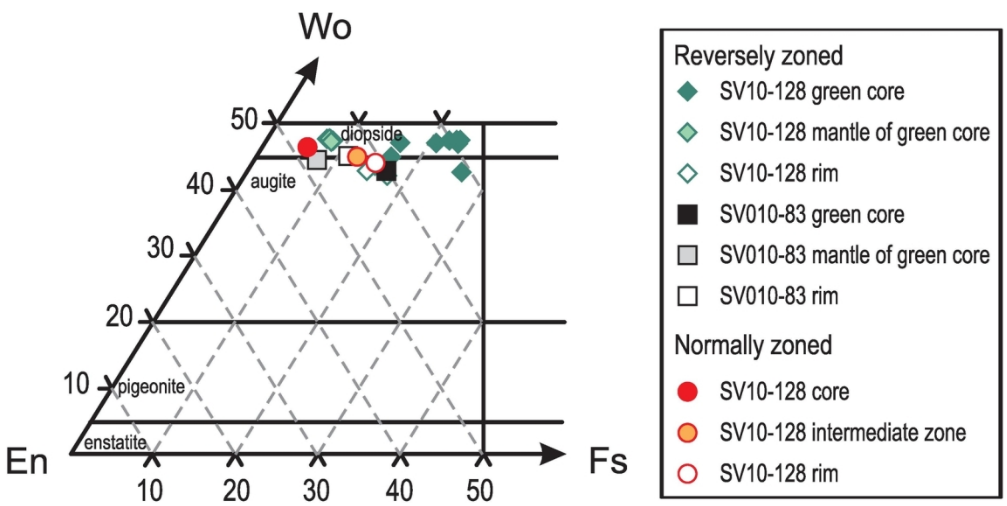

Fig. 4. (Colour online) Clinopyroxenes from the Stomanovo monzonite plotted in conventional Ca-Mg-Fe+Mn diagram (Morimoto et al. 1989).

139x68mm (300 x 300 DPI)

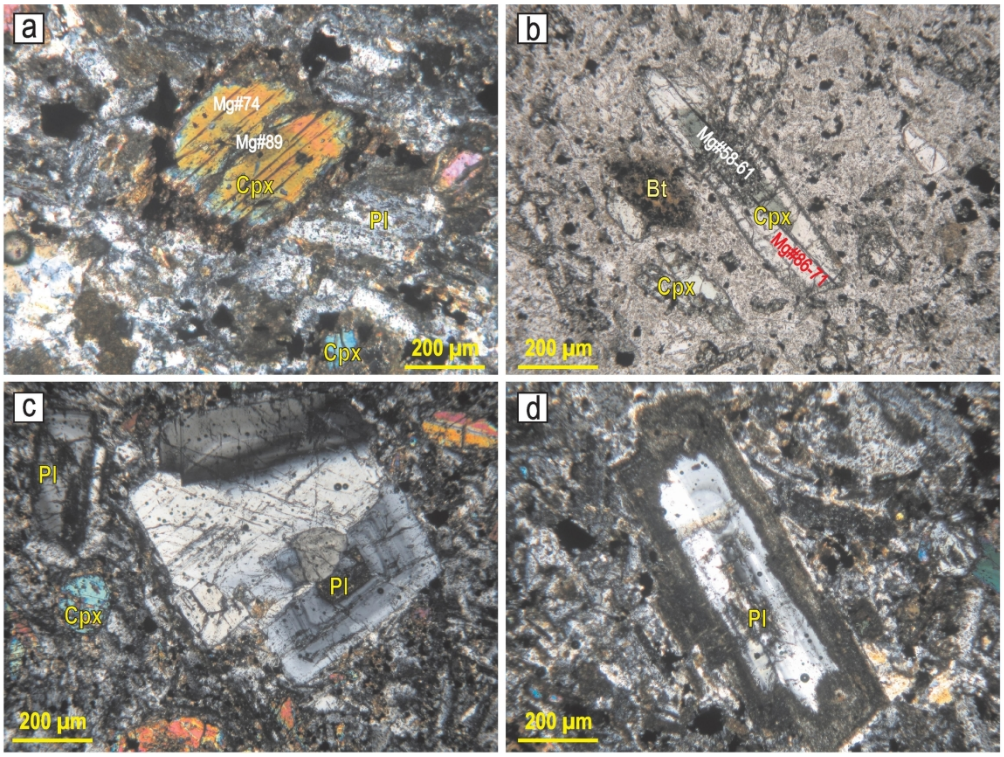

Fig. 5. (Colour online) Microphotographs showing zoning types of clinopyroxenes and plagioclase. (a) Normally zoned clinopyroxene with Mg-rich core and lower Mg rim; the lowest value is measured in the very thin rim. (b) Reversely zoned clinopyroxene with Fe-rich green core and Mg-rich rim. (c) Normally zoned plagioclase. (d) Sieve-textured plagioclase.

169x127mm (300 x 300 DPI)

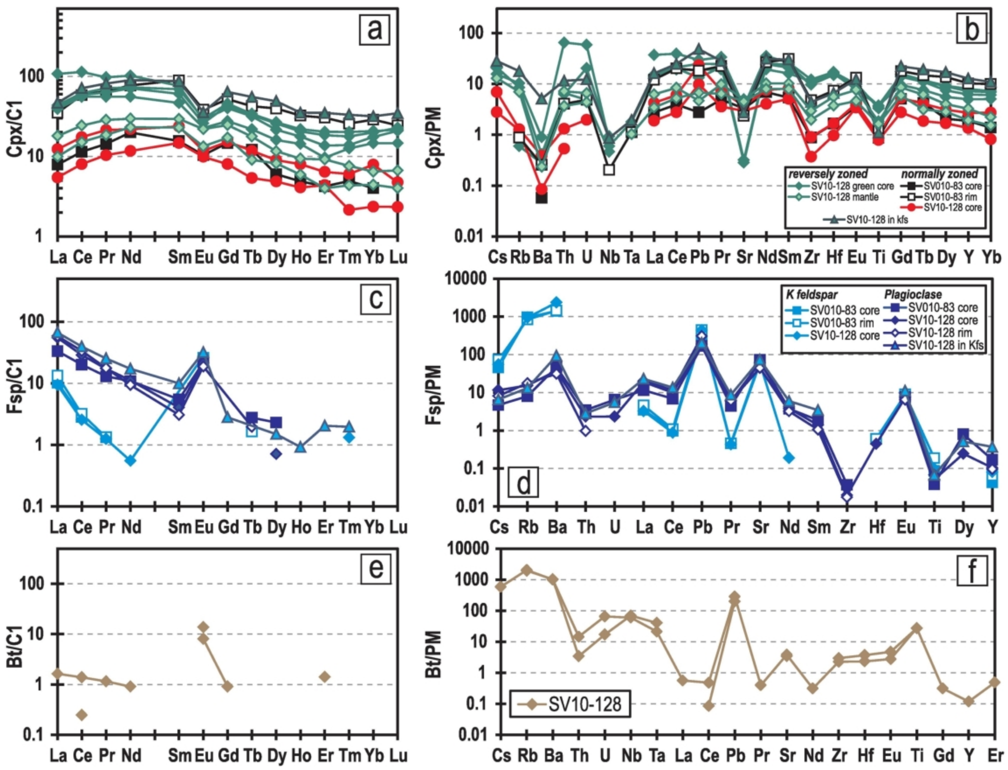

Fig. 6. (Colour online) Chondrite-normalized REE patterns (left panel) and primitive mantle-normalized multi-element patterns (right panel) for clinopyroxene (a, b), feldspars (c, d) and biotite (e, f). Chondrite and PM normalization values are from Sun & McDonough (1989).

169x128mm (300 x 300 DPI)

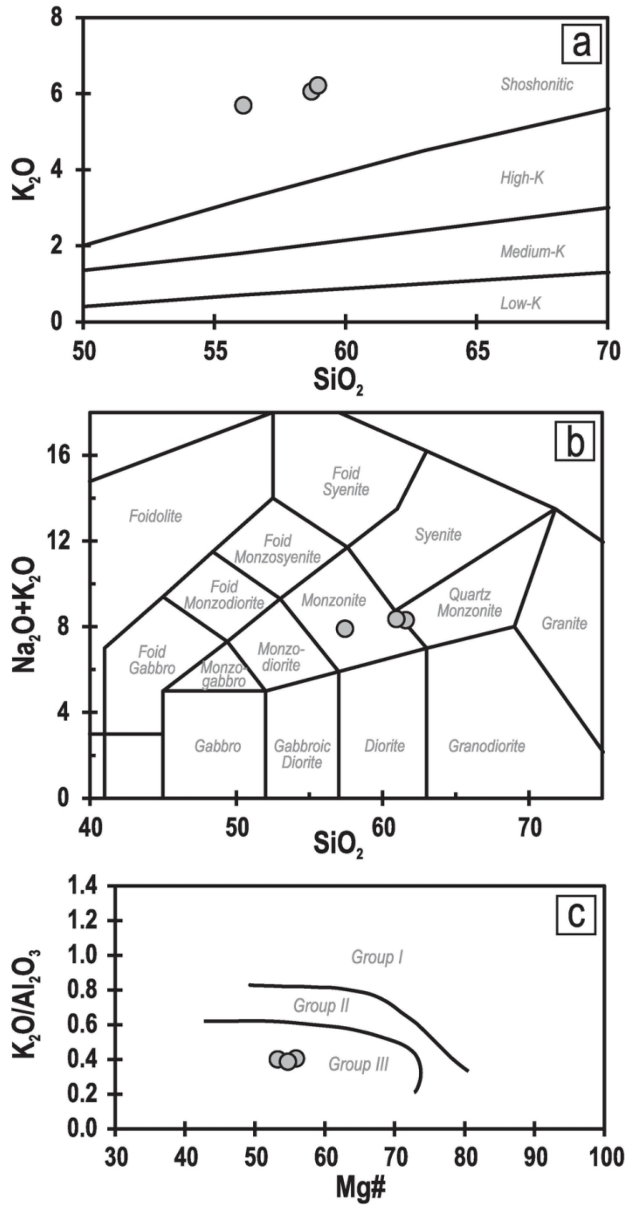

Fg. 7. Classification diagrams of the Stomanovo intrusion. (a) K2O vs. SiO2 classification diagram after Peccerillo and Taylor (1976). (b) Total Alkali vs.SiO2 (TAS) diagram (Middlemost, 1994).

80x156mm (300 x 300 DPI)

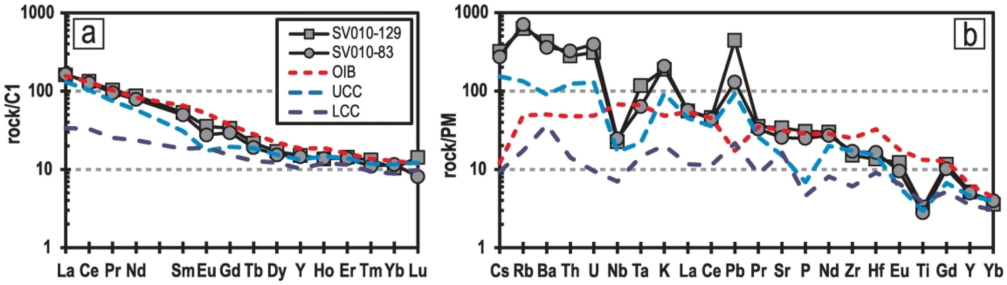

Fig. 8. (Colour online) Chondrite-normalized REE patterns: (8a) and primitive mantle-normalized multi-element patterns, (8b) for bulk rocks of the Stomanovo monzonite porphyry.
Normalizing values are from Sun & McDonough (1989). Average composition of OIB (Sun & McDonough, 1989) and upper and lower continental crust (Rudnick & Gao, 2003) are given for comparison.

168x46mm (300 x 300 DPI)

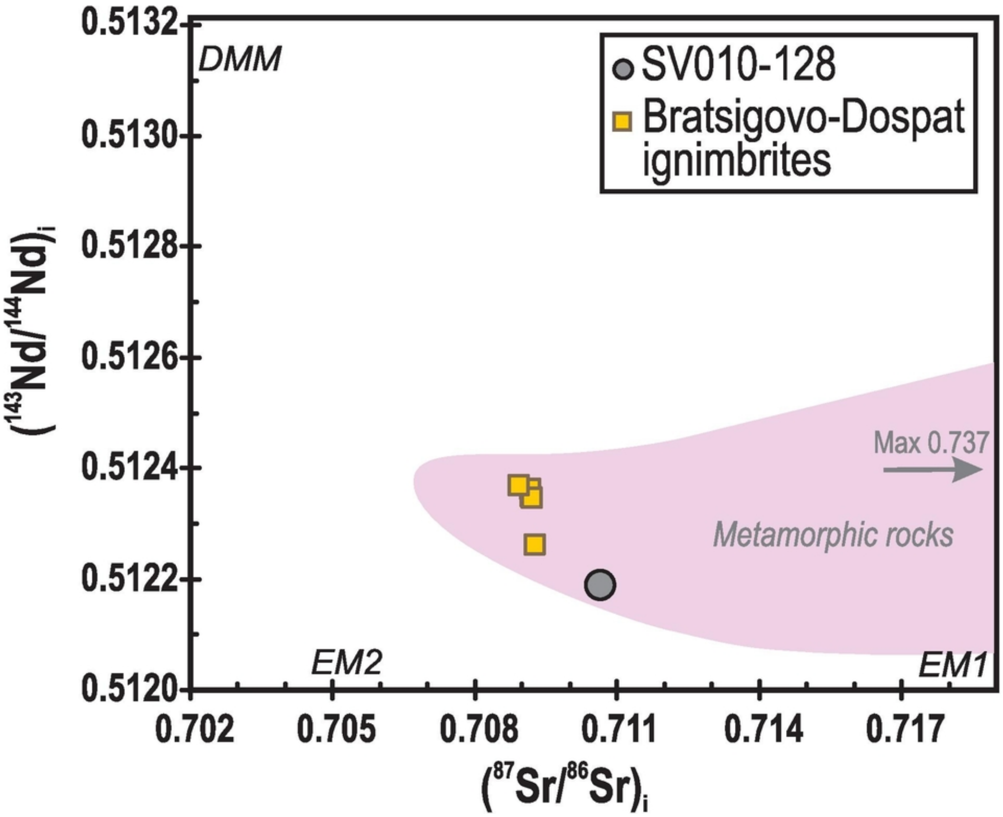

Fig.9. (Colour online) Sr and Nd isotopic compositions of the monzonite, compared with those of the host ignimbrites. Data for the Bratsigovo-Dospat ignimbrite are from Filipov et al. (2017).

81x65mm (300 x 300 DPI)

Marchev et al. Formation of ultrapotassic magma via crustal contamination and hybridization of mantle magma: an exampl

Supplementary table S1. U(-Th)-Pb isotope data for zircons of samples BD and SV

sample BD

			Isotope ratios							
Analysis_#	grain #		$^{207}Pb/^{206}Pb$	1σ	$^{206}Pb/^{238}U$	1σ	$^{207}Pb/^{235}U$	1σ	$^{208}Pb/^{232}Th$	1σ
12au20a04	1r	d	0.06039	0.00861	0.00499	0.00014	0.04155	0.00583	0.00215	0.00018
12au20a05	2r	*	0.04690	0.00628	0.00493	0.00012	0.03188	0.00422	0.00148	0.00011
12au20a06	4c	*	0.04788	0.00718	0.00501	0.00012	0.03308	0.00491	0.00147	0.00009
12au20a07	6r	*	0.04649	0.00709	0.00493	0.00011	0.03160	0.00479	0.00163	0.00011
12au20a08	7r	d	0.05173	0.00255	0.00491	0.00007	0.03500	0.00171	0.00147	0.00009
12au20a09	8cr	d	0.05534	0.00343	0.00495	0.00008	0.03779	0.00232	0.00155	0.00009
12au20a10	9cr	d	0.07796	0.00712	0.00490	0.00012	0.05269	0.00469	0.00194	0.00013
12au20a13	11r	*	0.04627	0.00661	0.00493	0.00013	0.03145	0.00443	0.00160	0.00014
12au20a14	12r	x	0.04458	0.00471	0.00852	0.00016	0.05238	0.00548	0.00268	0.00021
12au20a15	13r	x	0.05550	0.00277	0.06910	0.00110	0.52885	0.02591	0.02012	0.00151
12au20a16	11c	*	0.04825	0.00172	0.00490	0.00007	0.03262	0.00115	0.00156	0.00012
12au20a17	16c	d	0.03803	0.00634	0.00495	0.00010	0.02593	0.00430	0.00161	0.00013
12au20a18	16r	d	0.05935	0.00620	0.00497	0.00011	0.04068	0.00419	0.00175	0.00015
12au20a19	17r	d	0.06286	0.00508	0.00492	0.00010	0.04268	0.00338	0.00160	0.00014
12au20a20	18r	d	0.05218	0.00777	0.00490	0.00014	0.03528	0.00517	0.00154	0.00016
12au20b04	19r	d	0.07446	0.00583	0.00492	0.00010	0.05050	0.00387	0.00188	0.00011
12au20b05	20r	d	0.05401	0.00553	0.00495	0.00011	0.03684	0.00372	0.00187	0.00012
12au20b06	20c	*	0.04652	0.00561	0.00493	0.00010	0.03160	0.00377	0.00152	0.00008
12au20b07	21r	*	0.04676	0.00613	0.00495	0.00011	0.03190	0.00414	0.00161	0.00011
12au20b08	21c	d	0.05268	0.00212	0.00476	0.00007	0.03455	0.00137	0.00140	0.00007
12au20b09	23cr	*	0.04647	0.01114	0.00487	0.00013	0.03117	0.00744	0.00150	0.00010
12au20b10	24r	*	0.04617	0.00431	0.00491	0.00009	0.03128	0.00289	0.00149	0.00010
12au20b13	25r	*	0.04842	0.00626	0.00486	0.00011	0.03247	0.00416	0.00143	0.00011
12au20b14	26c	x	0.05478	0.00210	0.06730	0.00094	0.50832	0.01926	0.02010	0.00133
12au20b15	27r	d	0.10061	0.00735	0.00493	0.00011	0.06838	0.00484	0.00215	0.00015
12au20b16	31cr	d	0.08577	0.01614	0.00495	0.00020	0.05856	0.01079	0.00129	0.00018
12au20b17	33r	*	0.04645	0.00966	0.00495	0.00016	0.03170	0.00653	0.00135	0.00013
12au20b18	35r	*	0.05056	0.00623	0.00489	0.00013	0.03408	0.00413	0.00156	0.00013
12au20b19	35c	d	0.05796	0.00356	0.00489	0.00008	0.03905	0.00237	0.00146	0.00010
12au20b20	36r	x	0.05607	0.00232	0.06867	0.00101	0.53088	0.02166	0.02098	0.00193
12au20b21	36c	x	0.11383	0.00340	0.18619	0.00255	2.92228	0.08617	0.05653	0.00410
sample SV										
12au20c04	2r	d	0.07015	0.00496	0.00470	0.00009	0.04543	0.00315	0.00166	0.00009
12au20c05	3r	*	0.05070	0.00453	0.00467	0.00009	0.03266	0.00288	0.00134	0.00008
12au20c06	4c	x	0.05331	0.00120	0.04294	0.00053	0.31561	0.00719	0.01260	0.00062
12au20c07	6c	*	0.04651	0.00394	0.00468	0.00009	0.03002	0.00251	0.00134	0.00007
12au20c08	7r	*	0.04656	0.00626	0.00481	0.00011	0.03091	0.00412	0.00147	0.00011
12au20c09	10cr	d	0.07327	0.01072	0.00499	0.00018	0.05038	0.00718	0.00229	0.00020
12au20c10	11c	x	0.06305	0.00173	0.10656	0.00138	0.92637	0.02543	0.02928	0.00168
12au20c13	11r	d	0.31028	0.00903	0.14218	0.00219	6.08269	0.17171	0.20487	0.01351
12au20c14	13r	*	0.04666	0.00496	0.00481	0.00011	0.03095	0.00324	0.00141	0.00011
12au20c15	15r	*	0.04768	0.00781	0.00468	0.00015	0.03077	0.00495	0.00155	0.00015
12au21a04	18r	x	0.05497	0.00326	0.08940	0.00147	0.67761	0.03980	0.02842	0.00555
12au21a05	19c	d	0.29007	0.01397	0.00732	0.00017	0.29281	0.01296	0.00601	0.00030
12au21a06	20cr	x	0.05925	0.00165	0.10479	0.00139	0.85617	0.02391	0.02555	0.00107
12au21a07	21c	*	0.04559	0.00888	0.00474	0.00013	0.02978	0.00575	0.00130	0.00010
12au21a08	22cr	*	0.04656	0.00530	0.00485	0.00010	0.03113	0.00351	0.00137	0.00008
12au21a09	25r	d	0.09753	0.02013	0.00486	0.00027	0.06530	0.01301	0.00150	0.00024
12au21a10	26cr	*	0.04891	0.00413	0.00471	0.00009	0.03179	0.00265	0.00141	0.00008
12au21a13	27r	*	0.04595	0.00989	0.00482	0.00018	0.03057	0.00649	0.00144	0.00015
12au21a14	29c	x	0.06406	0.00174	0.12302	0.00163	1.08665	0.02951	0.03579	0.00208
12au21a15	29r	x	0.05544	0.00135	0.07499	0.00096	0.57328	0.01408	0.02252	0.00147
12au21a16	32r	d	0.06283	0.00845	0.00505	0.00015	0.04379	0.00577	0.00149	0.00015
12au21a17	35c	d	0.16926	0.00968	0.00605	0.00013	0.14130	0.00769	0.00285	0.00020
12au21a18	36c	d	0.05723	0.00977	0.00482	0.00015	0.03801	0.00639	0.00176	0.00017
12au21a19	34cr	d	0.35194	0.01348	0.00793	0.00016	0.38506	0.01361	0.00664	0.00050
12au21a20	37cr	x	0.05135	0.00715	0.04127	0.00101	0.29222	0.04027	0.01220	0.00146

Abbreviations: r, rim; c, core; rc, rim and core part;
* Analyses used for concordia age; d - discordant value; x - xenocryst

rho - error correlation of $^{206}Pb/^{238}U$ and $^{207}Pb/^{235}U$ defined as ($^{206}Pb/^{238}U$%err)/($^{207}Pb/^{235}U$%err)
Discordance rate: (1 - ($^{207}Pb/^{235}U$age)/($^{206}Pb/^{238}U$age))*100

le from the Stomanovo monzonite, Bulgaria

rho	Age estimates (Ma)								Discordance
	$^{207}Pb/^{206}Pb$	1σ	$^{206}Pb/^{238}U$	1σ	$^{207}Pb/^{235}U$	1σ	$^{208}Pb/^{232}Th$	1σ	%
0.20	617.5	281.2	32.1	0.9	41.3	5.7	43.5	3.7	*22.3*
0.18	43.9	292.7	31.7	0.8	31.9	4.2	29.9	2.1	*0.6*
0.16	92.1	322.3	32.2	0.8	33.0	4.8	29.8	1.9	*2.4*
0.15	23.0	330.2	31.7	0.7	31.6	4.7	32.8	2.2	*-0.3*
0.29	273.6	109.2	31.6	0.5	34.9	1.7	29.8	1.9	*9.5*
0.26	425.8	133.0	31.8	0.5	37.7	2.3	31.3	1.8	*15.6*
0.28	1145.8	171.5	31.5	0.8	52.1	4.5	39.2	2.6	*39.5*
0.19	11.9	311.7	31.7	0.8	31.4	4.4	32.3	2.8	*-1.0*
0.18	0.1	161.5	54.7	1.1	51.8	5.3	54.1	4.2	*-5.6*
0.32	432.3	107.1	430.7	6.6	431.0	17.2	402.7	29.9	*0.1*
0.41	111.8	82.1	31.5	0.4	32.6	1.1	31.4	2.4	*3.4*
0.12	0.1	0.0	31.8	0.7	26.0	4.3	32.5	2.6	*-22.3*
0.21	580.1	212.2	32.0	0.7	40.5	4.1	35.4	3.1	*21.0*
0.26	703.5	163.3	31.7	0.6	42.4	3.3	32.4	2.8	*25.2*
0.19	293.5	308.3	31.5	0.9	35.2	5.1	31.0	3.2	*10.5*
0.27	1053.7	150.6	31.6	0.7	50.0	3.7	38.0	2.2	*36.8*
0.22	371.4	215.6	31.8	0.7	36.7	3.6	37.8	2.4	*13.4*
0.17	24.6	266.4	31.7	0.7	31.6	3.7	30.7	1.7	*-0.3*
0.17	36.8	287.3	31.8	0.7	31.9	4.1	32.6	2.3	*0.3*
0.37	315.1	88.8	30.6	0.4	34.5	1.4	28.4	1.5	*11.3*
0.11	22.2	492.7	31.3	0.9	31.2	7.3	30.4	2.0	*-0.3*
0.20	6.3	210.5	31.6	0.6	31.3	2.8	30.1	1.9	*-1.0*
0.18	119.8	279.4	31.3	0.7	32.4	4.1	28.9	2.2	*3.4*
0.37	403.3	82.9	419.8	5.7	417.3	13.0	402.3	26.3	*-0.6*
0.32	1635.3	129.9	31.7	0.7	67.2	4.6	43.4	3.1	*52.8*
0.22	1332.9	326.3	31.8	1.3	57.8	10.4	26.0	3.7	*45.0*
0.16	20.8	435.3	31.8	1.0	31.7	6.4	27.3	2.6	*-0.3*
0.22	220.8	262.1	31.4	0.8	34.0	4.1	31.5	2.6	*7.6*
0.27	527.8	129.5	31.4	0.5	38.9	2.3	29.5	2.1	*19.3*
0.36	454.6	89.7	428.2	6.1	432.4	14.4	419.6	38.2	*1.0*
0.46	1861.5	52.9	1100.7	13.9	1387.7	22.3	1111.5	78.5	*20.7*
0.28	932.8	138.6	30.2	0.6	45.1	3.1	33.5	1.9	*33.0*
0.22	227.0	194.1	30.0	0.6	32.6	2.8	27.1	1.6	*8.0*
0.54	342.1	50.2	271.0	3.3	278.5	5.6	253.2	12.4	*2.7*
0.23	24.1	191.7	30.1	0.6	30.0	2.5	27.0	1.5	*-0.3*
0.17	26.7	294.3	31.0	0.7	30.9	4.1	29.6	2.1	*-0.3*
0.25	1021.6	270.7	32.1	1.1	49.9	6.9	46.3	4.1	*35.7*
0.47	709.8	57.3	652.8	8.1	665.7	13.4	583.4	33.0	*1.9*
0.55	3522.3	44.2	857.0	12.3	1987.8	24.6	3767.1	226.7	*56.9*
0.22	31.7	236.8	30.9	0.7	30.9	3.2	28.5	2.2	*0.0*
0.20	82.6	349.0	30.1	1.0	30.8	4.9	31.3	3.1	*2.3*
0.28	410.8	127.0	552.0	8.7	525.3	24.1	566.5	109.0	*-5.1*
0.52	3418.0	72.9	47.0	1.1	260.8	10.2	121.2	5.9	*82.0*
0.47	576.4	59.4	642.4	8.1	628.0	13.1	509.9	21.0	*-2.3*
0.14	0.1	390.7	30.5	0.9	29.8	5.7	26.2	2.0	*-2.3*
0.18	26.9	252.8	31.2	0.7	31.1	3.5	27.6	1.6	*-0.3*
0.28	1577.3	343.5	31.2	1.7	64.2	12.4	30.2	4.8	*51.4*
0.23	143.4	187.2	30.3	0.6	31.8	2.6	28.6	1.6	*4.7*
0.18	0.1	445.5	31.0	1.2	30.6	6.4	29.2	3.1	*-1.3*
0.49	743.5	56.3	747.9	9.4	746.9	14.4	710.8	40.6	*-0.1*
0.52	429.8	52.9	466.1	5.8	460.1	9.1	450.2	29.2	*-1.3*
0.23	702.3	262.9	32.5	1.0	43.5	5.6	30.2	3.0	*25.3*
0.39	2550.4	92.8	38.9	0.9	134.2	6.8	57.5	4.1	*71.0*
0.19	499.7	337.8	31.0	1.0	37.9	6.3	35.5	3.5	*18.2*
0.57	3715.4	57.1	50.9	1.0	330.8	10.0	133.8	10.0	*84.6*
0.18	256.5	292.0	260.7	6.3	260.3	31.6	245.2	29.2	*-0.2*

Marchev et al. Formation of ultrapotassic magma via crustal contamination and hybridization of mantle magma: an example fr

Supplementary table S2. Representative major element composition and structural form

	SV010-83 2-1 Pl core	SV010-83 2-2 Pl intermediate zone	SV010-83 2-3 Pl rim	SV010-83 3-1 Sa core	SV010-83 3-2 Sa rim	SV10-128 3-1 Pl core	SV10-128 3-2 Pl intermediate zone	SV10-128 3-3 Pl intermediate zone	SV10-128 3-4 Pl rim
SiO_2	51.10	56.51	61.58	64.04	65.26	54.87	55.82	55.24	56.89
TiO_2	n.d.	n.d.	n.d.	n.d.	n.d.	0.02	0.05	0.00	0.03
Al_2O_3	31.34	28.81	23.89	19.63	19.27	28.47	27.75	27.93	27.06
FeO	0.52	0.46	0.25	0.09	0.23	0.41	0.35	0.34	0.56
MnO	0.20	0.06	0.08	0.00	0.10	0.02	0.02	0.02	0.02
MgO	0.00	0.01	0.07	0.00	0.00	0.05	0.05	0.04	0.07
CaO	13.89	10.10	5.29	0.36	0.23	11.30	9.88	10.59	9.22
Na_2O	3.53	5.71	8.59	2.94	2.81	5.18	5.84	5.56	6.12
K_2O	0.37	0.39	0.50	11.84	13.02	0.59	0.70	0.58	0.32
BaO	0.03	0.05	0.00	1.45	0.67	n.d.	n.d.	n.d.	n.d.
SrO	0.38	0.07	0.65	0.00	0.05	n.d.	n.d.	n.d.	n.d.
	101.36	102.17	100.90	100.35	101.64	100.91	100.46	100.30	100.29
An	67.0	48.3	24.7	1.8	1.1	52.9	46.4	49.6	44.6
Ab	30.8	49.4	72.5	26.2	24.1	43.9	49.7	47.1	53.6
Or	2.1	2.2	2.8	69.4	73.6	3.3	3.9	3.2	1.8
Cn	0.1	0.1	0.0	2.6	1.2	0.0	0.0	0.0	0.0
Si	2.310	2.497	2.730	2.941	2.959	2.466	2.511	2.492	2.553
Ti	0.000	0.000	0.000	0.000	0.000	0.001	0.002	0.000	0.001
Al	1.670	1.500	1.248	1.062	1.030	1.508	1.471	1.485	1.431
Fe	0.020	0.017	0.009	0.003	0.009	0.015	0.013	0.013	0.021
Mn	0.008	0.002	0.003	0.000	0.004	0.001	0.001	0.001	0.001
Mg	0.000	0.001	0.005	0.000	0.000	0.003	0.003	0.003	0.005
Ca	0.673	0.478	0.251	0.018	0.011	0.544	0.476	0.512	0.443
Na	0.309	0.489	0.738	0.262	0.247	0.451	0.509	0.486	0.532
K	0.021	0.022	0.028	0.694	0.753	0.034	0.040	0.033	0.018
Ba	0.001	0.001	0.000	0.026	0.012	0.000	0.000	0.000	0.000
Sr	0.010	0.002	0.017	0.000	0.001	0.000	0.000	0.000	0.000

Abbreviations. Pl - plagioclase; Sa - sanidine *om the Stomanovo monzonite, Bulgaria*

ula (O=8) of feldspar from the Stomanovo U-K monzonite

SV10-128	SV10-128	SV10-128	SV10-128	SV10-128
5-3	5-4	5-1	5-5	5-6
Pl	Pl	Sa	Sa	Sa
core	rim	core	intermediate zone	rim
55.16	56.04	63.84	63.55	64.03
0.03	0.00	0.31	0.00	0.00
28.52	27.09	18.88	19.13	19.10
0.53	0.39	0.19	0.17	0.33
0.03	0.00	0.02	0.02	0.00
0.03	0.00	0.00	0.11	0.02
10.72	9.71	0.29	0.26	0.42
5.63	6.24	2.58	2.35	2.89
0.37	0.28	12.82	12.79	11.66
n.d.	n.d.	n.d.	1.27	1.54
n.d.	n.d.	n.d.	0.10	0.17
101.02	99.75	98.93	99.75	100.16
50.2	45.5	1.4	1.3	2.1
47.7	52.9	23.1	21.0	26.0
2.1	1.6	75.5	75.4	69.1
0.0	0.0	0.0	2.3	2.8
2.472	2.534	2.957	2.947	2.952
0.001	0.000	0.011	0.000	0.000
1.507	1.444	1.031	1.046	1.038
0.020	0.015	0.007	0.007	0.013
0.001	0.000	0.001	0.001	0.000
0.002	0.000	0.000	0.008	0.001
0.515	0.470	0.014	0.013	0.021
0.489	0.547	0.232	0.211	0.258
0.021	0.016	0.758	0.757	0.686
0.000	0.000	0.000	0.023	0.028
0.000	0.000	0.000	0.003	0.005

Marchev et al. Formation of ultrapotassic magma via crustal contamination and hybridization of mantle magma: an example fr

Supplementary table S3. Representative major element composition and structural form

	Biotite				Ilmenite	
	SV10-128	**SV010-83**	**SV010-83**		**SV010-83**	**SV010-83**
	in sanidine	core	rim			
SiO_2	36.25	37.97	36.86	**SiO_2**	0.03	0.11
TiO_2	6.37	5.64	6.12	**TiO_2**	42.55	42.69
Al_2O_3	14.22	13.90	13.26	**Al_2O_3**	0.00	0.03
Cr_2O_3	0.14	0.00	0.03	**Cr_2O_3**	0.15	0.00
FeO	11.84	11.37	12.28	**FeO**	49.48	47.73
MnO	0.11	0.09	0.12	**MnO**	6.04	6.40
MgO	16.47	18.12	17.32	**MgO**	0.51	0.23
CaO	0.05	0.02	0.00	**CaO**	0.08	0.47
Na_2O	0.40	0.39	0.33	**Na_2O**	0.00	0.07
K_2O	9.18	9.73	10.04	**K_2O**	0.02	0.02
BaO	1.46	0.54				
F	0.68	3.18	3.29			
SO_3	0.33	0.09				
Cl	0.22	0.23	0.30			
Total	97.72	101.27	99.95		98.84	97.66
Mg#	**71.3**	**74.0**	**71.5**			
H_2O*	3.68	2.59	2.43			
Subtotal	101.07	103.77	102.38			
O=F,Cl	0.34	1.39	1.45			
Total	100.73	102.38	100.93			
Si	5.359	5.481	5.431			
Al(IV)	2.478	2.365	2.303			
Al(VI)	0.000	0.000	0.000			
Ti	0.708	0.612	0.678			
Cr	0.016	0.000	0.003			
Fe	1.464	1.373	1.513			
Mn	0.014	0.011	0.015			
Mg	3.630	3.899	3.804			
Ca	0.008	0.003	0.000			
Na	0.115	0.109	0.094			
K	1.731	1.791	1.887			
Ba	0.085	0.031	0.000			

rom the Stomanovo monzonite, Bulgaria

ula (O=22) of biotite and ilmenite from the Stomanovo U-K monzonite

Marchev et al. Formation of ultrapotassic magma via crustal contamination and hybridization of mantle magma: an

Supplementary table S4. Representative trace element (LA-ICP-MS) concentrations of fel

	SV010-83			SV10-128					
	Sa	Sa	Pl	Pl	Pl	Pl	Sa	Bt	Bt
	core	rim	core	core	rim	in Sa			
Sc	<1.84	<1.73	<2.68	<1.12	<1.19	<1.50	<1.32	17	17
V	<0.62	<0.77	<1.16	<0.74	<0.63	0.87	<0.56	505	503
Cr	<15.25	<14.03	<17.68	<8.77	<10.67	<11.83	<9.88	125	37
Co	<0.40	<0.35	0.91	0.36	0.39	<0.33	<0.23	66	95
Ni	6.36	<12.84	<15.70\	<7.27	<10.44	<8.32	<9.74	85	100
Rb	605	536	5.08	9.78	11.19	8.34	599	1295	1244
Sr	1234	1442	1526	1303	938	1548	1244	81	72
Y	0.20	0.30	0.77	0.48	0.44	1.69	0.37	0.54	<0.22
Zr	<0.15	<0.16	0.41	0.22	0.20	<0.17	<0.19	25	33
Nb	<0.19	<0.19	<0.15	<0.13	<0.14	<0.15	<0.09	43	50
Cs	1.46	2.32	0.15	0.37	0.26	0.21	1.76	19	n.d.
Ba	9836	10110	330	265	218	655	16503	7067	7168
La	2.43	3.14	7.90	13.04	13.83	15.81	2.23	0.39	<0.16
Ce	1.74	1.94	12.27	17.63	20.48	24.15	1.56	0.85	0.15
Pr	<0.10	0.13	1.23	1.64	1.68	2.41	0.12	0.11	<0.09
Nd	<0.65	<0.39	5.09	5.21	4.37	8.06	0.26	0.42	<0.54
Sm	<0.76	<0.85	0.84	0.62	0.47	1.52	<0.31	<0.31	<0.51
Eu	1.39	1.50	1.27	1.23	1.09	1.86	1.59	0.47	0.80
Gd	<0.30	<0.32	<0.80	<0.49	<0.38	0.58	<0.56	0.19	<0.41
Tb	<0.08	0.06	0.10	<0.06	0.07	<0.07	<0.06	<0.06	<0.07
Dy	<0.36	<0.27	0.59	0.18	<0.23	0.38	<0.22	<0.15	<0.30
Ho	<0.11	<0.08	<0.07	<0.04	<0.04	0.05	<0.03	<0.06	<0.08
Er	<0.21	<0.42	<0.62	<0.14	<0.21	0.34	<0.20	0.23	<0.35
Tm	<0.04	<0.07	<0.11	<0.03	<0.05	0.05	0.03	<0.05	<0.08
Yb	<0.49	<0.30	<1.05	<0.27	<0.21	<0.36	<0.39	<0.28	<0.31
Lu	<0.06	<0.04	<0.16	<0.05	<0.03	<0.08	<0.05	<0.04	<0.08
Hf	<0.16	0.19	<0.35	0.14	<0.30	<0.15	<0.16	0.72	1.14
Ta	<0.10	<0.06	<0.16	<0.04	<0.04	<0.05	0.05	0.87	1.66
Pb	60	82	31	35	57	38	81	53	37
Th	<0.13	<0.08	0.29	0.20	0.08	0.24	<0.05	1.23	0.29
U	<0.05	<0.05	0.14	0.05	<0.07	0.12	<0.09	1.37	0.36

example from the Stomanovo monzonite, Bulgaria

ldspars and phlogopite in the the Stomanovo U-K monzonite

Marchev et al. Formation of ultrapotassic magma via crustal contamination and hybridization of mantle magma: an example from the Stomanovo monzonite, Bulgaria

Supplementary figure S5. Assimilation and fractional crystallization (AFC) models

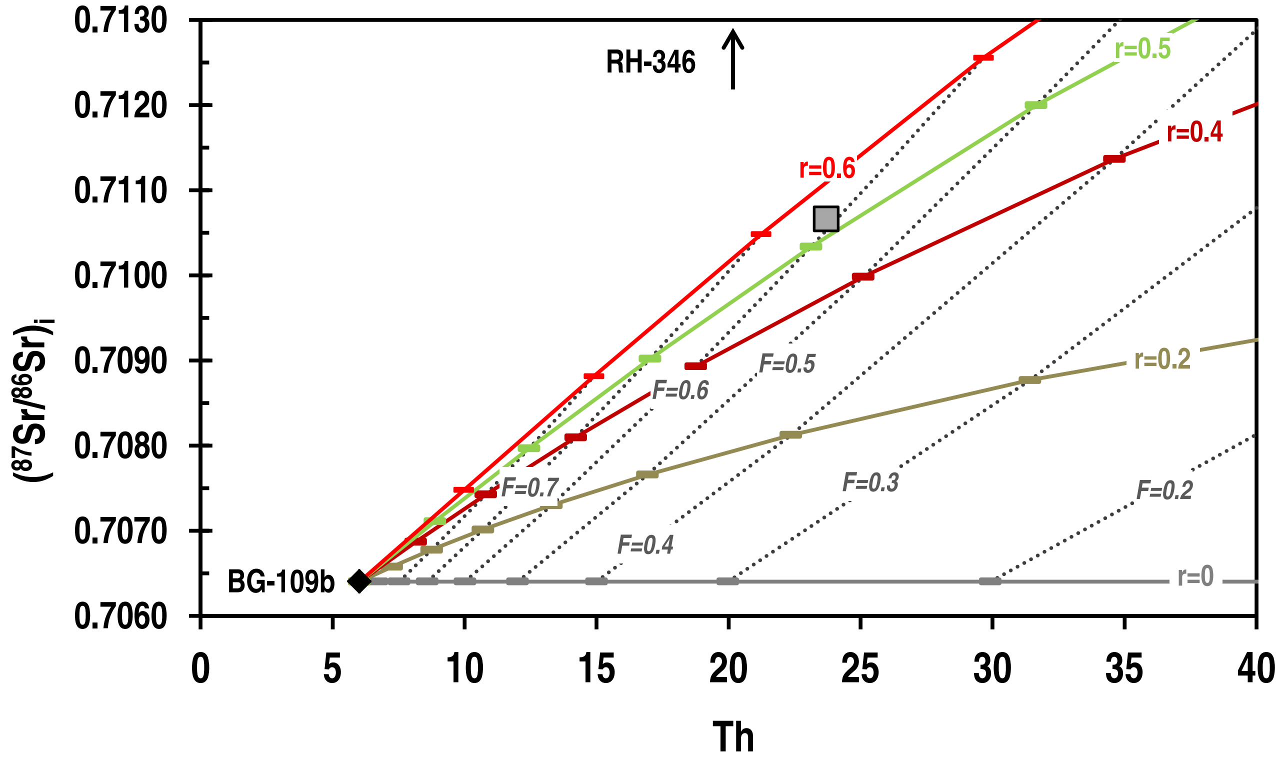

Assimilation and fractional crystallization (AFC) models using equations of De Paolo (1981) for the Stomanovo monzonite. Basic end-member is absarokite (sample Bg109b, Sr=366.9, Th=6.02, $^{87}Sr/^{86}Sr$=0.70641) from Kirchenbaur et al. (2012). The composition of the Carboniferous gneiss contaminant material (sample RH346, Sr=108.1, Th=19.73, $^{87}Sr/^{86}Sr$=0.72820) is taken from Cornelius (2008).
(r) is ratio of assimilated material to crystallized material. Marks on the AFC curves (F) represent the ratio of magma mass to original magma mass. Bulk partition coefficient used in the modeling are: DSr = 1.2, DTh = 0.004.
The AFC curves are plotted with AFC-Modeler (Keskin, 2013).

References:

Cornelius, N. K. 2008. UHP metamorphic rocks of the Eastern Rhodope Massif, NE Greece: new constraints from petrology, geochemistry and zircon ages. PhD thesis. Mainz, Johannes Gutenberg University, 164 pp. http://doi.org/10.25358/openscience-4327

Keskin, M. 2013. AFC-Modeler: a Microsoft® Excel© workbook program for modelling assimilation combined with fractional crystallization (AFC) process in magmatic systems by using equations of DePaolo (1981). Turkish Journal of Earth Sciences 22, 304–319.